Structure of an Internal Bore and Dissipating Gravity Current as Revealed by Raman Lidar

STEVEN E. KOCH,* PAUL B. DORIAN,† R. FERRARE,‡ S. H. MELFI,* WILLIAM C. SKILLMAN,* AND D. WHITEMAN#

*NASA/Goddard Space Flight Center, Laboratory for Atmospheres, Greenbelt, Maryland
†General Sciences Corporation, Laurel, Maryland
‡Universities Space Research Association, NASA/Goddard Space Flight Center, Greenbelt, Maryland
#NASA/Goddard Space Flight Center, Laboratory for Terrestrial Physics, Greenbelt, Maryland

(Manuscript received 16 April 1990, in final form 31 August 1990)

ABSTRACT

Detailed moisture observations from a ground-based Raman lidar and special radiosonde data of two disturbances associated with a dissipating gust front are presented. A synthesis of the lidar data with conventional meteorological data, in conjunction with theoretical calculations and comparison to laboratory studies, leads to the conclusion that the disturbances seen in both the lidar and accompanying barograph data represent a weak gravity current and an associated undular bore. The disturbances display excellent coherence over hundreds of kilometers upstream of the lidar site. Bore formation occurs at the leading edge of the gust front coincidentally with the rapid weakening of the gravity current. Analysis suggests that the bore was generated by the collapse of the gravity current into a stable, nocturnal inversion layer, and subsequently propagated along this wave guide at nearly twice the speed of the gravity current.

The Raman lidar provided detailed measurements of the vertical structure of the bore and its parent generation mechanism. A mean bore depth of 1.9 km is revealed by the lidar, whereas a depth of 2.2 km is predicted from hydraulic theory. Observed and calculated bore speeds were also found to agree reasonably well with one another ($\sim \pm 20\%$). Comparison of these observations with those of internal bores generated by thunderstorms in other studies reveals that this bore was exceedingly strong, being responsible for nearly tripling the height of a surface-based inversion that had existed ahead of the bore and dramatically increasing the depth of the moist layer due to strong vertical mixing. Subsequent appearance of the relatively shallow gravity current underneath this mixed region resulted in the occurrence of an elevated mixed layer, as confirmed with the special radiosonde measurements.

A synthesis of the lidar and radiosonde observations indicates that bore-induced parcel displacements attenuated rapidly at the same height as the level of strongest wave trapping predicted from the theory of Crook. This trapping mechanism, which is due to the existence of a low-level jet, results in a long-lived bore, and seems to be a common phenomenon in the environment of thunderstorm-generated bores and solitary waves. Despite the weakening of a capping inversion by this strong and persistent bore, analysis indicates that the 30-min averaged lifting of 0.7 m s^{-1} was confined to a too shallow layer near the surface to trigger deep convection, and could only produce scattered low clouds as deduced from the lidar measurements.

1. Introduction

Recent developments in numerical modeling and remote sensing have demonstrated that deep convection frequently develops within narrow zones of strong convergence in the lower atmosphere. Numerical studies utilizing idealized models and mesoscale models show that thermally direct circulations induced by topographic effects and/or discontinuities in the surface energy budget can provide ascent throughout a relatively deep layer ($\sim$10–50 cm s^{-1} in a 2–4 km deep layer); thus requiring *sufficient time* ($\sim$1–4 h) to lift layers to their levels of free convection (Koch 1988). On the other hand, much stronger circulations produced by boundary-layer phenomena (such as gravity currents, bores, and solitary waves) may be capable of directly triggering deep convection because of the presence of 1–15 m s^{-1} vertical velocities—provided that this layer of ascent is *sufficiently deep.* This second class of circulation systems appears to be especially effective at initiating storms within 30 min when the systems "collide" with one another (Purdom 1982; Wilson and Schreiber 1986; Carbone et al. 1990).

Gravity currents are primarily horizontal flows generated by density differences and involve essentially pure mass transport, consisting of the advection of

Corresponding author address: Dr. Steven E. Koch, Code 912 Bldg. 22, Room 322, NASA/Goddard Space Flight Center, Greenbelt, MD 20771.

dense, cold fluid toward the leading edge (head) of the current and a return flow within the elevated head. Their kinetic energy arises from the conversion of the potential energy of the cold air as it spreads horizontally under the influence of gravity. Thunderstorm outflows, sea breezes, katabatic wind systems, and possibly some cold fronts display strong similarities to gravity currents observed in the laboratory (Simpson 1987). Their passage is characterized by an abrupt decrease in surface temperature, a sudden jump in pressure hydrostatically linked to the cooling, and a sharp windshift and increased gustiness caused by the horizontal pressure gradient and vertical mixing.

The presence of low-level stratification is particularly favorable for the evolution of gravity currents into a host of other phenomena: turbulent bores, followed by undular bores, and ultimately solitary waves or solitons (Christie et al. 1978, 1979; Simpson 1987). An internal undular bore is a type of gravity wave disturbance that *propagates* on low-level inversions and does not transport dense fluid, at least not in its pure form. Numerical and laboratory experiments show that bores are typically generated as gravity currents encounter strong stratification near the ground (e.g., Maxworthy 1980; Crook 1988; Smith 1988; Rottman and Simpson 1989; Haase and Smith 1989b), in particular: 1) as a disturbance generated on the stable layer, which then propagates ahead of the gravity current, 2) as the gravity current is modified upon interacting with the stable layer, or 3) as the gravity current collapses entirely into the stable layer. Christie et al. (1978), Shreffler and Binkowski (1981), and others have observed that bore-like disturbances, formed as the result of the interaction of a cold thunderstorm outflow with a preexisting temperature inversion, can travel hundreds of kilometers from their place of origin. Presence of a suitably thick layer of weak stratification above this surface-based stable layer can suppress the vertical radiation of wave energy above the stable layer, thus, providing a partial explanation for the long lifetimes and large amplitudes observed for some atmospheric bores (Crook 1986). Other mechanisms for trapping wave energy proposed by Crook (1988) require particular configurations of vertical shear.

Bores and gravity currents can cause substantial upward displacements of air parcels in the lower troposphere and are thereby capable of generating clouds and deep convection. Recent observations by Fulton et al. (1990) and numerical analysis by Haase and Smith (1989b) suggest that intermediate structures between a gravity current and a smooth undular bore are also possible. These phenomena display the appearance of an undular bore, yet carry a remnant of the cold air originally contained in the gravity current within a closed circulation at the leading edge of the bore; namely, one or more large amplitude solitary waves. Smith (1988) and Fulton et al. (1990) emphasize the difficulty of distinguishing bores from gravity currents in observations, despite the fact that the two phenomena are dynamically dissimilar, in part because of the wide spectrum of phenomena between the pure bore and gravity current structures that can occur. Furthermore, bores and gravity currents are both accompanied by a windshift into the direction of movement of the disturbance and a net cooling in the lower atmosphere consistent with the sustained surface pressure increase that follows the initial abrupt pressure rise. However, cooling associated with a gravity current is due to horizontal advection, whereas adiabatic ascent is the cause of cooling in the case of a bore. Thus, pronounced *surface* cooling is not characteristic of bores; in fact, temperature often rises as the result of turbulent downward mixing of warmer air from above the inversion in the case of bores.

Previous observational studies of atmospheric gravity currents and bores have employed photography, surface synoptic and mesonetwork measurements, instrumented towers, pilot balloons, instrumented aircraft, acoustic sounders, satellite imagery, doppler radar, and aerosol lidars (McAllister 1968; Marks 1974; Goff 1976; Bedard and Saunders 1978; Christie et al. 1978, 1979; Shreffler and Binkowski 1981; Carbone 1982; Hasse and Smith 1984; Doviak and Ge 1984; Shapiro 1984; Shapiro et al. 1985; Seitter and Muench 1985; Nakane and Sasano 1986; Carbone et al. 1990; Fulton et al. 1990). The present study seeks to exploit the powerful capabilities of the Raman lidar (Melfi and Whiteman 1985; Melfi et al. 1989) to investigate the structure and dynamics of a weakening gravity current and the bore that it generated. This instrument does not require strong vertical gradients or turbulent fluctuations in temperature or moisture to probe the atmosphere, a constraint that can make it difficult to study bores with acoustic sounders and radars (Marks 1974); though they can readily detect gravity currents. Moreover, the Raman lidar can measure in a vertical column of the atmosphere to depths unachievable with towers and surface systems. Furthermore, the Raman lidar can obtain data at levels below that possible with Doppler radars and can sample the atmosphere at much higher intervals than can be provided by either aircraft or balloons. Previous studies that have utilized this instrument have demonstrated its capability to provide mixing ratio profiles with an uncertainty of only ±5%–10% at 2-min intervals and a vertical resolution of 100 m to altitudes of 5–7 km. Its only technical disadvantages seem to be its inability to provide any information above cloud base and the fact that it is presently limited to nighttime operation. These studies have shown that moisture features seen in the lidar data are either in agreement with those appearing in collocated radiosonde data, or are consistent with the radiosonde data but indicate rapid changes in moisture that cannot be resolved by the radiosondes. Melfi et al. (1989) have further demonstrated the ability of the lidar to observe the shape and slope of warm

and cold fronts, detailed structures in the frontal zones, and even, by inference, the nature of transverse frontal circulations; thus, suggesting that a similar approach could be applied to investigate the structure and airflow within gravity currents and bores.

The present study utilizes conventional surface meteorological analyses, special rawinsonde data, spectral and bandpass filter analysis of barograph data, and infrared satellite imagery to complement the Raman lidar observations of two disturbances: a weak gravity current and an internal bore associated with a thunderstorm gust front. Resulting analyses are also critically compared against theoretical predictions concerning these phenomena. This study has four primary objectives:

1) demonstrate the ability of the Raman lidar system to measure the vertical and temporal moisture variations associated with the bore and gravity current, using other supporting data to corroborate the space–time continuity of these mesoscale disturbances.
2) Employ these synthesized data in the determination of the origin and dynamic nature of the mesoscale disturbances.
3) Make quantitative comparisons between the lidar-derived vertical structure of the bore/gravity current system and that predicted from theory.
4) Relate the bore-induced vertical parcel displacements to observed cloud development.

The lidar data discussed in this paper were collected on the evening of 8–9 June 1987 at NASA/Goddard Space Flight Center (GSFC) in Greenbelt, Maryland, as part of a field campaign to assess the capabilities of the Raman lidar (Melfi et al. 1989). Procedures for processing the lidar and supporting data are described in section 2. The lidar observations and an accompanying barograph trace made at the lidar site are presented in section 3. Two major disturbances seen in both of the datasets are described. The nature of these phenomena is further explored with satellite, surface, and radiosonde data in section 4. The results of these analyses are synthesized and then compared with laboratory and theoretical studies of gravity currents and bores in section 5 to arrive at an understanding of the dynamic character of the two disturbances, the mesoscale structure of the ambient atmosphere, and the relationship of the disturbances to cloud formation. A discussion of the bearing that this study has on the problem of cloud and storm initiation by boundary-layer disturbances appears in section 6, followed by a summary in section 7.

2. Data processing

A thorough description of the Raman lidar system and recent modifications appear in Melfi and Whiteman (1985) and Melfi et al. (1989). Briefly, the Raman lidar consists of a laser beam that is pointed vertically and a telescope that collects the scattered laser light. Beamsplitters on the receiver partition the received energy into three channels, one sensitive to Raman scattering by water-vapor molecules, a second sensitive to Raman scattering by nitrogen, and the third sensitive to scattering by molecules and aerosols at the laser wavelength. Both analog-to-digital (ADC) and photon counter (PC) data are generated from the output, and the ADC data are smoothed from their original 15-m vertical resolution to approximately 100-m resolution. These data are generally used from near the surface to almost 2 km, whereas the higher quality PC data are used at higher altitudes where receiver saturation due to intense backscattering is not a problem. Calibration of the lidar data is performed using a least-squares fit between the derived mixing ratio and an independent measurement from a rawinsonde launched concurrently at the lidar site. The displayed moisture variable is mixing ratio, because the ratio of Raman scattering by water vapor to that by nitrogen is nearly proportional to the water-vapor mixing ratio. This calibration procedure is conducted no more than once daily, since the alignment of the telescope remains unchanged during this period. Nocturnal moisture profiles are acquired continuously once every two minutes and are then composited to form an image that shows the time versus height variation of moisture during a single period of operation. In the present case, data were collected from 2144 EDT (0144 UTC) on 8 June until 0500 EDT (0900 UTC) on 9 June 1987.

An additional product generated from the lidar data is the aerosol backscattering ratio. This quantity is computed by taking the ratio of backscatter at the laser wavelength (the sum of Rayleigh scattering from molecules and Mie scattering from aerosols) to the Raman nitrogen backscatter. According to Melfi et al. (1989), large ratios indicate the presence of optically thick clouds. Infrared (11.6 μm) imagery from the GOES satellite is compared in this study to the time–height variation of the aerosol backscattering ratio. The purpose of this intercomparison is to assess the role that mesoscale phenomena observed by the lidar—as deduced from undulations in the heights of moisture surfaces—may have played in the formation of clouds. The satellite data were navigated at 0000 UTC using an objective landmark identification technique on the AOIPS/2 interactive meteorological processing system at GSFC (Hasler and desJardins 1987). Residual errors in image registration indicated that the navigations were as accurate as the data could allow ($\pm$8 km). These images were then remapped to a Lambert Conic Conformal projection and smoothed to facilitate comparisons with the surface analyses. Finally, the images were subjected to a grey-level slicing technique that enhances the coldest cloud tops and permits easier identification of the active convective regions.

Conventional hourly surface data from National

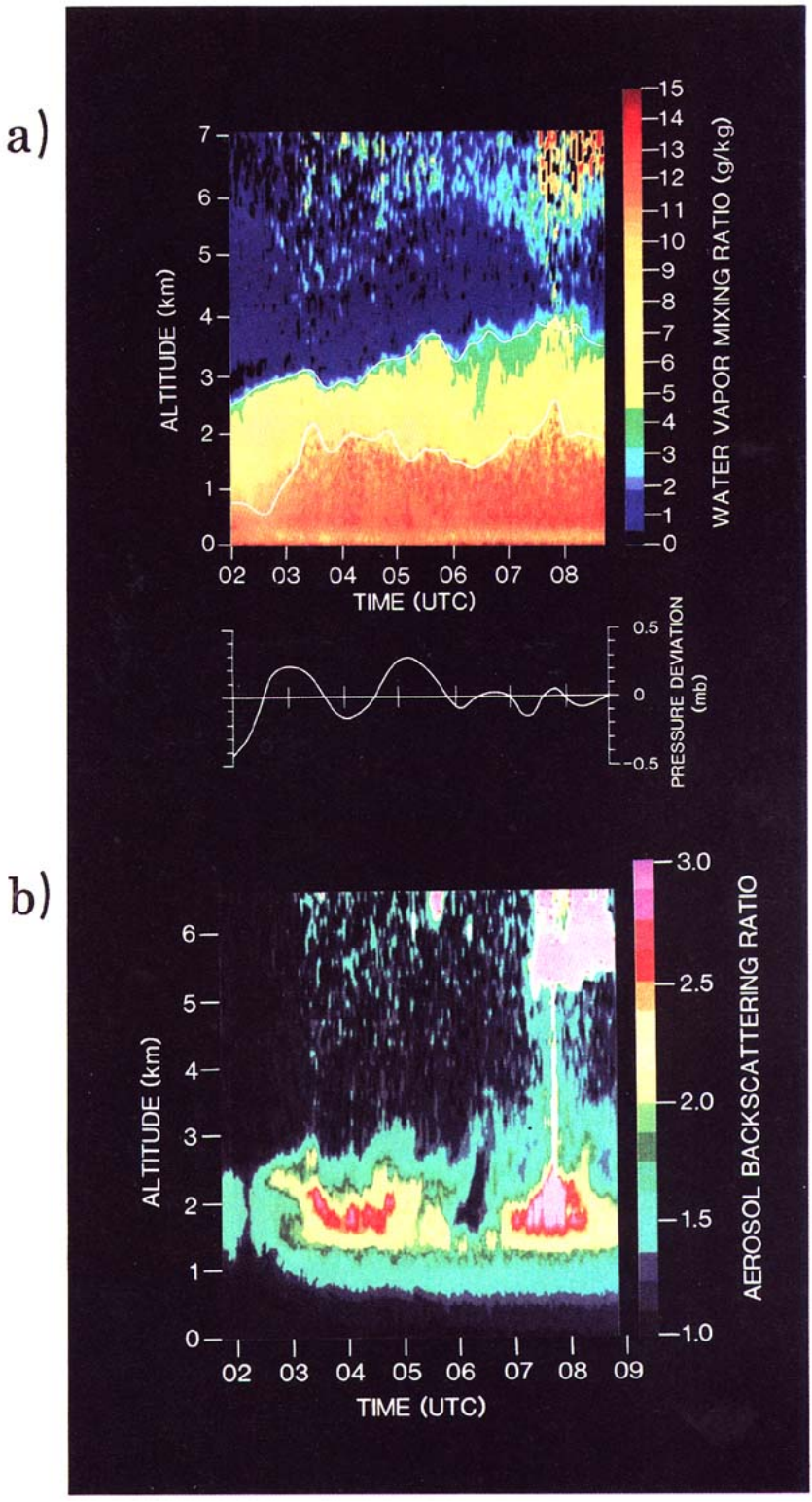

FIG. 1. Color-coded time–height images of (a) water-vapor mixing ratio (top) and (b) aerosol backscattering ratio (bottom), along with collocated pressure trace (middle). Linear trend in the digitized barograph data has been removed. Color images were constructed by compositing 216 separate soundings acquired every 2 min with the ground-based Raman lidar at Goddard Space Flight Center on 8–9 June 1987. White curves emphasize height variation of 3 and 10 g kg^{-1} mixing ratio surfaces following application of low-pass filter (see text). Thick haze or scattered cloud debris is implied to exist at aerosol backscattering ratios > 2.5 (red/purple regions), whereas optically thick clouds are indicated by purple/white regions with ratios > 3.0.

Weather Service synoptic stations were analyzed on the GEMPAK system (desJardins and Petersen 1983) in order to detect the gust front, follow its evolution, and determine its relation to the disturbances seen in the lidar data. Strip charts from the synoptic barograph network within a 12-state area surrounding the lidar site in Maryland were manually digitized at 15-min intervals. An autospectral analysis of the barograph data was then conducted to reveal the dominant periods of disturbances seen in these data, for the dual purposes of making comparisons with spectra of the lidar data and of designing an appropriate bandpass filter for further analysis of the disturbances. Isochrone and time–space cross-section analyses of the resulting perturbation pressure disturbances and the gust front were then made to obtain estimates of their movements.

The digitized pressure data were analyzed with the weighted autocovariance method of power spectrum analysis incorporating Tukey lag windows (Jenkins and Watts 1968). A spectral peak was considered significant only when (i) it was separated from any adjacent peak by a frequency interval exceeding the Tukey spectral bandwidth, (ii) the peak was not the obvious consequence of leakage or variance problems, and (iii) the peak passed the 95% confidence level as determined by comparison to the estimated white noise variance level. This methodology is the same as that employed by Koch and Golus (1988) in a study of gravity waves.

The fast Fourier transform (FFT) technique was applied to the lidar time series of the height of the water-vapor mixing ratio surfaces in order to isolate the dominant periods in the moisture spectrum. High-frequency noise in this 2-min resolution data was reduced with a low-pass binomial filter prior to applying the FFT analysis. The raw FFT spectral estimates were then smoothed and a measure of significance was computed using a first-order autoregressive process to model the noise (Jenkins and Watts 1968). Peaks had to pass the 95% confidence level with respect to this red noise process to be considered significant.

A series of four special radiosonde ascents made approximately every 90 min at GSFC during the evening of 8–9 June 1987 were also available for this study. The moisture data from the sondes were used to validate the lidar measurements, whereas the temperature data were used as input to an isentropic cross-section analysis for the dual purposes of defining the background atmospheric state and determining changes associated with the passage of the disturbances revealed by the lidar and barograph data. These analyses were then synthesized with the other results obtained from the lidar and surface analyses in order to ascertain the dynamic character of the disturbances and to allow for quantitative comparisons with laboratory and theoretical studies.

3. Lidar and collocated barograph observations

The time–height composited display of water-vapor mixing ratio observed by the Raman lidar is shown in Fig. 1a. The observations cover the time period from 0200 to 0845 UTC during the evening of 8–9 June 1987. The color bar gives the relationship between color and mixing ratio, and extends from almost 0 (black) to 15 g kg^{-1} (red). A nonlinear color scale has been applied, whereby the 5–9 g kg^{-1} range has been stretched. This was done to emphasize the rapid decrease of moisture with height in the altitude range of 2.5–3.5 km, which is the top of the moist layer. In addition, two white curves appear on this image, representing smoothed variations in the 3 (upper) and 10 g kg^{-1} (lower) surfaces. These curves emphasize the vertical coherency in water-vapor fluctuations observed by the lidar, while reducing the amount of high-frequency noise. The "nearly equal ripple" low-pass filter of Kaiser and Reed (1977) was used to eliminate features with periods shorter than 15 min and to leave unaffected features with periods longer than 35 min. This particular filter design was governed by the results from the autospectral analysis of the lidar data, which indicated important signals only at these larger periods (this is explained below).

Three pronounced "humps" are evident prior to 0600 at the top of the moist layer, as defined by the 3 g kg^{-1} line: the first at 0315, the second at 0445, and the third at 0530 (all times are given to ±15-min accuracy because of the filter application). Similar variations are evident in the lower troposphere, as emphasized by the 10 g kg^{-1} line: (i) a rapid uplifting of this surface to 2.1 km at 0315 from an earlier height of only ~0.7 km; (ii) a broad, double-humped disturbance characterized by peaks at 0400 and 0445; and (iii) a weak, isolated disturbance at 0530. Each of the individual humps at this level, with the single exception of that at 0400, occurs at essentially the same times as the disturbances in the 3 g kg^{-1} surface. Fluctuations after 0600 are not so well correlated between these two levels and display a loss of clarity resulting from greatly enhanced diffusion, as suggested by the rapid decrease in vertical moisture gradients at the top of the moist layer immediately following the passage of the second hump at 0445.

The collocated pressure trace at GSFC following removal of the linear trend in the data during the 0200–0845 interval is also depicted in Fig. 1. The trace exhibits features quite similar to those appearing in the lidar data: (i) a major disturbance peaking at 0300 (only 15 min prior to the first hump seen in the lidar data), hereafter denoted as PP1 (pressure perturbation 1); (ii) a similar perturbation at 0500, hereafter denoted as PP2; and (iii) two minor disturbances during the diffusive episode following 0600. Considering the relatively poor time resolution and lag response of the barograph (each about 15 min), the good correlation between events PP1 and PP2 in the pressure trace and the events at 0315 and 0445 in the lidar display suggests that the two sensors were observing the same thing. These phenomena are the topic of concern in this paper.

The aerosol backscattering ratio is shown in Fig. 1b. The data used to generate this display were normalized to unity in regions of the atmosphere where scattering was assumed to be due to molecular effects only. These regions have been color-coded black. Regions that exceed the assumed level of molecular scattering are displayed as colors. The green regions represent a scattering ratio of 2, defined as aerosol scattering equal to molecular scattering. Purple represents a scattering ratio of ≥ 3 (or aerosol scattering equal to twice the molecular scattering), indicating the presence of optically thick clouds (Melfi et al. 1989). Thus, the small purple areas appearing occassionally above 6 km likely represent cirrus clouds, whereas the vertical streak of purple at 0745 represents optically thick, low clouds just above the 2-km level. Thick haze or scattered, thin, low clouds can be implied to have first formed at ~0315 within the crest of disturbance PP1. Notice that this haze region descends from 2.1 km at 0315 to 1.5 km at 0345, paralleling the behavior of both the 10 g kg^{-1} mixing ratio surface (Fig. 1a) and the pressure tendency following passage of PP1. This haze region then ascends again to reach a peak at 0445 in association with the appearance of disturbance PP2. Also notice that whenever there is noise in the lidar-observed *mixing ratio* data above 5 km, the aerosol backscattering ratio below that height exceeds ~2.5, since thick haze, and particularly clouds, strongly attenuate the lidar signal.

Spectral analysis of the barograph data at Silver Spring, Maryland,[1] (located only 12 km from the lidar site) is shown in Fig. 2 for comparison with the lidar spectrum of the height of the 3 g kg^{-1} surface. *This spectral intercomparison provides additional support for the notion that the lidar and barograph were sensing the same atmospheric phenomena.* The most significant peak in the pressure spectrum is at a period of 141 min. [Since only two disturbances (PP1 and PP2) were prominent in the barograph data, the "period" in the pressure spectrum does not refer to a truly periodic phenomenon, but rather the temporal separation between these two events.] Similarly, the primary peak in the moisture spectrum is at a period of 128 min, although a second significant peak is found at 67 min. The average period computed from the pressure spectra of the six stations nearest the lidar site (Fig. 5) was found to be 152 min (2.54 h). It is also noteworthy that lidar spectral power falls off sharply to a relative minimum at $f = 0.027$ min^{-1}, corresponding to a period of 37 min, and then returns to rather strong levels at $f > 0.045$ min^{-1} (period < 22 min). These spectral characteristics, which were also seen in the other mixing ratio surfaces, are interpreted as evidence for the existence of undesirable "noise" in the lidar data at periods smaller than ~20 min. Such information was therefore used in the design of the low-pass filter, which was applied to the mixing ratio surfaces (Fig. 1a).

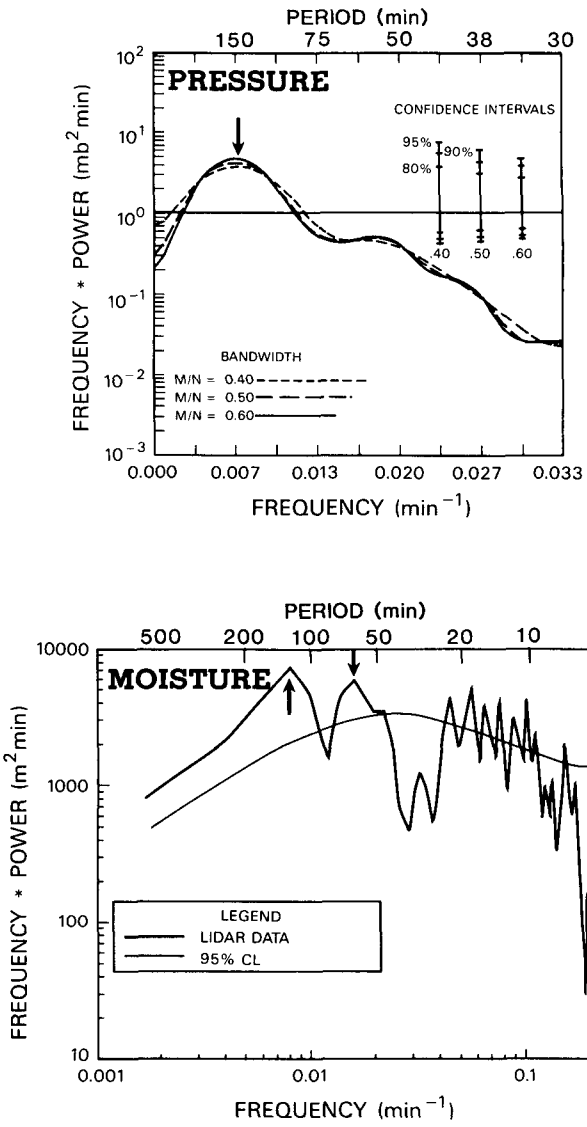

FIG. 2. Power spectra of surface pressure from station SIL (top) and of the lidar-observed height of the 3 g kg^{-1} mixing ratio line (bottom) during the episode 0200–0800 UTC 9 June 1987. Pressure spectrum was computed from 15-min data using weighted autocovariance method for various lag windows (M = maximum autocorrelation lag, N = data record length); confidence intervals are displayed about a horizontal line denoting the expected value of the white noise variance. Moisture spectrum was computed from 2-min data using FFT approach; 95% confidence interval denoted by curve was computed for a first-order autoregressive process. The peaks denoted with an arrow in each spectrum are significant at the 95% level; frequencies of these peaks are 0.0078 min^{-1} and 0.0150 min^{-1} in the moisture spectrum, and 0.0071 min^{-1} in the pressure spectrum.

The observations presented raise several interesting questions to be addressed in this paper.

1) First and foremost is why there is such a close relationship between perturbations seen in the pressure

[1] This barograph trace was selected over the one located precisely at the lidar site because its signal strength was slightly stronger.

trace and the depth of the moist layer. Hypotheses will be postulated upon assuming that (i) the disturbances are essentially hydrostatic phenomena, so that pressure variations represent purely mass variations; and that (ii) water vapor can act as a tracer of the fluctuations in the mass (potential temperature) field in the absence of condensation and evaporation.

2) Another point that needs addressing is why the second disturbance in the 10 g kg^{-1} surface (at 0400–0445) was either only weakly apparent in the 3 g kg^{-1} surface at 0445 or was phase-shifted to 0530. Likewise, the fact that the pressure trace appears more consistent with changes at the higher level is a mystery. We will also address the question of why strong diffusion or mixing followed the passage of PP2.

3) While the strong correlation between the lidar and pressure data increases our confidence in the details appearing in the lidar display, additional confirmation that these features represent actual mesoscale phenomena in the atmosphere is needed using other kinds of supporting data. It remains to be shown whether the disturbances seen in the lidar and pressure data exhibit strong time–space continuity across a broad region, not just at a single point.

4) There is also the issue of whether additional analysis can identify the likely origin and cause of the disturbances, and what role precipitation processes may have played in their occurrence.

4. Analysis of satellite, surface, and rawinsonde data

Other data are analyzed in this section in an attempt to address those questions just raised about the lidar and barograph data. Satellite data are first studied for the purpose of relating the cloud patterns to the aerosol backscattering ratio and the mesoscale environment. The surface data are then analyzed to define the gust front associated with a nearby squall line and its possible relationship to PP1 and PP2, and additionally, to determine the motion and possible origin of these disturbances. Finally, the rawinsonde data are analyzed so as to compare its moisture profiles with the lidar displays, to help define the background atmospheric state, and to assess the effects of the disturbances on the atmosphere.

a. Satellite imagery

A four-panel display of the infrared imagery processed in the manner described earlier is shown in Fig. 3. Regions of cold blackbody temperatures are indicative of high cloud tops often associated with deep convection. These regions appear as grey-level enhancement surrounded by white. The only such region at 0000 UTC 9 June 1987 (top left panel) is that depicting an intense squall line spanning the entire state of Pennsylvania, with cloud tops as cold as 208 K (corresponding to heights of 14 km). This system had just finished producing considerable damaging winds and large hail through eastern Ohio and a large portion of Pennsylvania. Only a band of scattered cirrus debris from the storm system has reached the lidar site (GSC) at this time (thin cirrus clouds are depicted as white regions with no enhancement, corresponding to higher blackbody temperatures resulting from the lower emissivity of such clouds). The squall line dramatically weakens in the subsequent two hours, as indicated by the warming of the cloud tops. A solid cirrostratus shield produced from the mesoscale convective system covers the lidar site at 0200. Further breakup of the system is apparent by 0400 and thereafter.

Comparison of the 0200 satellite image with the aerosol backscattering ratio (Fig. 1b) shows that at the lidar site no other clouds exist below the "cirrus anvil", which foretells of the approach of the convective system. By contrast, the satellite image at 0400 shows a thin band of thicker clouds, extending in an arc from northwest of IAD, down and across the District of Columbia (DCA) to GSC, and then back north again in a discontinuous fashion to just south of Philadelphia (PHL). The aerosol backscattering ratio display at this time indicates a layer of thick haze or scattered, thin, low clouds near the 2-km level under the high cloud deck seen by the satellite. The last satellite image (at 0530) indicates only a band of high clouds at the lidar site, again consistent with the aerosol backscattering ratio display indicating broken clouds at and above 6 km. *Thus, in general there appears to be strong relationships between features seen in the lidar data and clouds evident in the satellite imagery.* This result was confirmed with the hourly surface reports of cloud height and amount from Baltimore (BWI) and nearby stations (Fig. 4).

b. Surface analyses

The surface data are studied with several objectives in mind. They are helpful for following the evolution of disturbances PP1 and PP2, the gust front, and the mesoscale conditions surrounding them. Useful estimates of the phase velocities of these phenomena are also obtained with the surface data. An attempt is made to isolate the origin of the disturbances and to provide a tentative understanding of their dynamics by combining these data with the lidar observations.

1) Evolution of mesoscale disturbances

The surface analyses (Fig. 4) are made at or near the same times as the satellite analyses in Fig. 3. The most obvious feature present at 0000 UTC is a pronounced wind discontinuity at the leading edge of the cold outflow from the Pennsylvania squall line, as de-

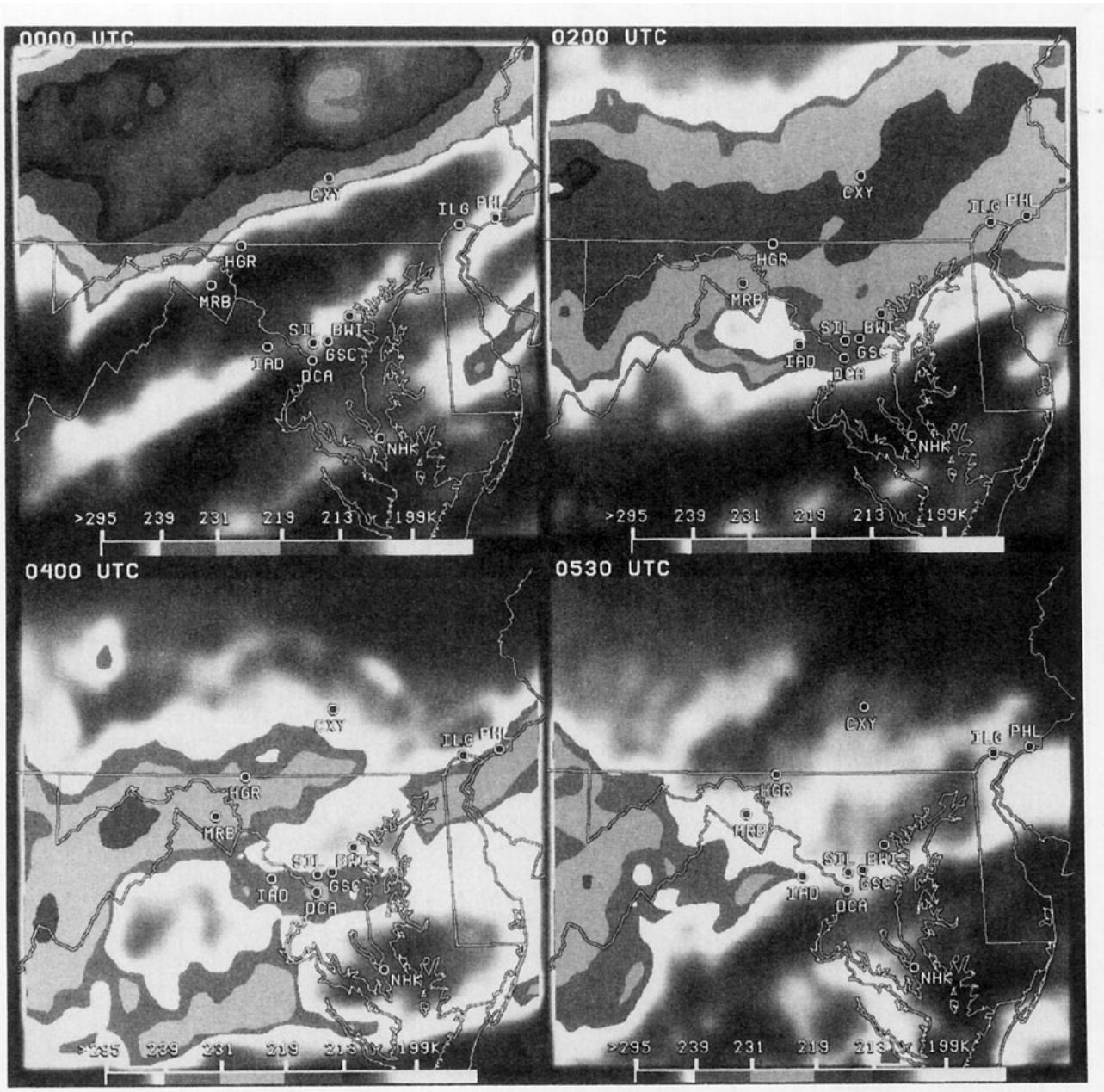

FIG. 3. Sequence of enhanced infrared GOES imagery on 9 June 1987. Grey bar indicates blackbody temperatures corresponding to values defined by familiar "MB" enhancement curve. Lidar is located at station GSC (Goddard Space Flight Center) in Maryland.

picted by the frontal symbols in Fig 4. This system fits the classic definition of a gust front, in which a sharp increase in wind speed occurs coincidentally with a sustained wind shift, a rapid temperature drop, and a sudden pressure jump. *The term "gust front" as used here will refer specifically to the temperature drop line associated with passage of the thunderstorm outflow boundary.* Hourly synoptic data were used to determine the temperature drop times but were supplanted whenever possible by between hour "specials" that gave the times of dramatic windshifts to gusty, northwesterly winds in an attempt to be more precise about the actual times of temperature drops associated with the gust front (sudden temperature changes are not reported in special observations unless associated with synoptic frontal passages). This definition is not a universal one; e.g., the study by Fulton et al. (1990), which benefited from the use of 1-min resolution mesonetwork data, defined the gust front as the wind discontinuity, without regard to a temperature drop.

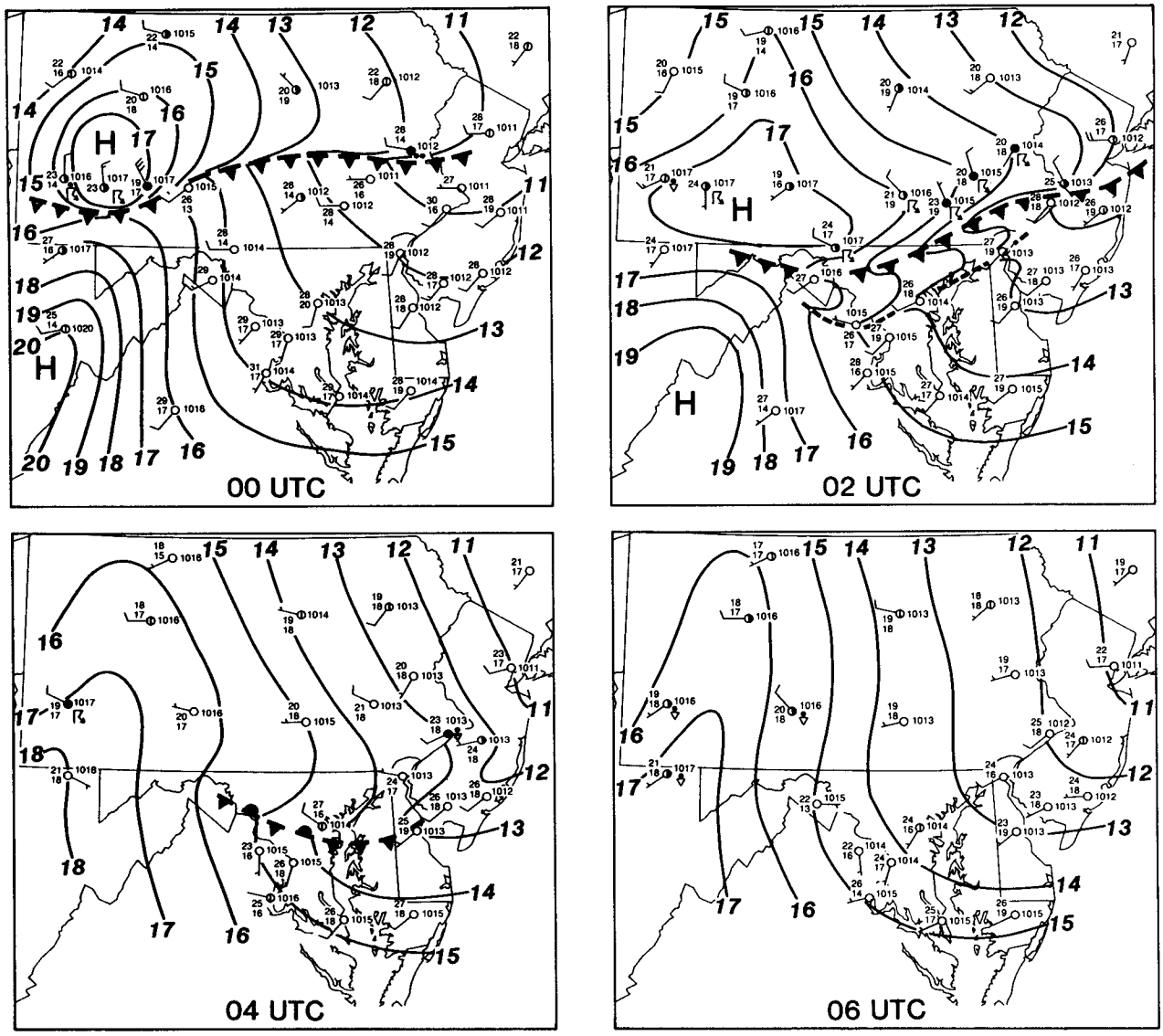

FIG. 4. Sequence of surface analyses at same times as those appearing in Fig. 3, with the exception of the last panel. Leading edge of cold thunderstorm outflow (gust front) and leading edge of pressure disturbance PP1 are depicted by frontal and trough symbols, respectively. Isobars are shown analyzed at intervals of 0.1 kPa. Shown plotted at stations are dry-bulb and dewpoint temperatures (°C), winds (long barb = 5 m s^{-1}), altimeter setting (1011 = 101.1 kPa), low cloud cover, and present weather. Existence of PP1 was guided by barograph time series analysis (e.g., Fig. 6).

Several other important features appear in the surface analyses in Fig. 4. A mesohigh pressure cell appears in the southwestern part of the state at the center of the cold air at 0000 UTC—a hydrostatic consequence of the cold outflow temperatures. The mesohigh and associated windshift (from southwesterlies to strong northwesterlies) both weaken throughout the subsequent 6-h period as the squall line system breaks down, becoming essentially imperceptible by 0600. A new feature represented by a trough line appears on the scene at 0200 UTC. Although this feature—the leading edge of pressure disturbance PP1—cannot be resolved by the hourly surface data distribution, the barograph time series from stations distributed throughout the region (dots in Fig. 5) clearly show the formation and development of this pronounced event (Fig. 6). The existence of PP1 was first verified with local barograph traces surrounding the lidar site. Its direction of propagation (determined as discussed below) was then used to backtrack the position of PP1 as a function of time to Harrisburg (CXY) and other stations distributed throughout southern Pennsylvania. A similar proce-

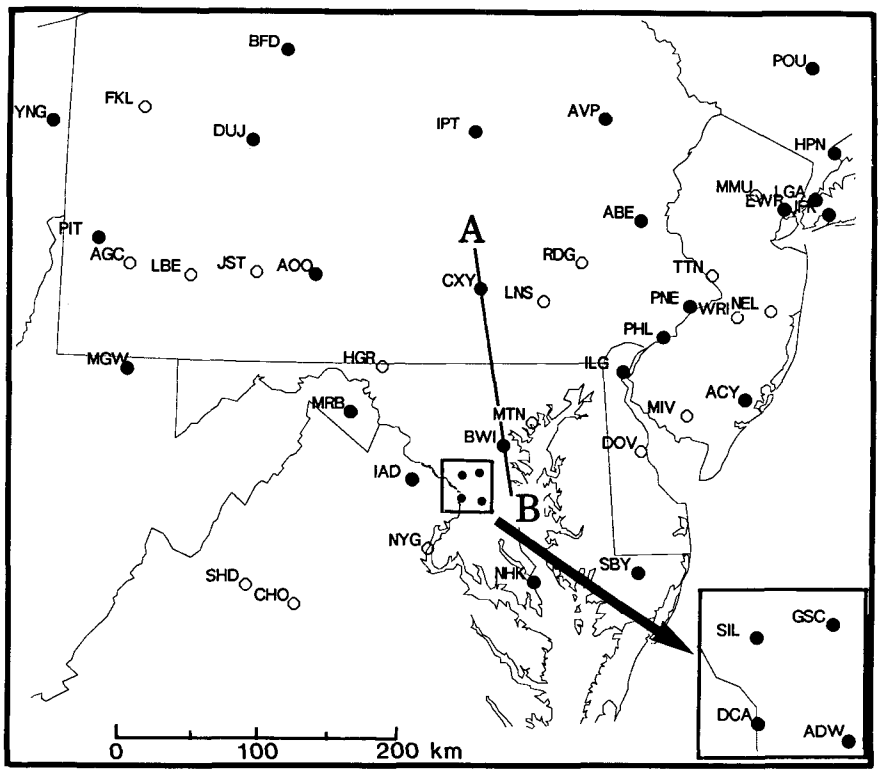

FIG. 5. Locations of stations referred to in text, as well as cross-sectional path A–B used in construction of Fig. 8. Stations depicted with dots represent sites where barograph data were available. Supplementary barographs are located at SIL (National Weather Service Headquarters in Silver Spring) and GSC (Goddard Space Flight Center); lidar is located at the latter site.

dure was followed with regard to disturbance PP2. Although the >100-km distance separating the cluster of barograph sites in central Maryland from CXY might seem to make this method questionable, the quasi-two-dimensional nature of disturbances PP1 and PP2 allowed information from such stations as MRB and ILG to fill in this gap.

The most important conclusion that can be drawn from the time series in Fig. 6 is that *the initial wind discontinuity was always coincident with the leading edge of pressure disturbance PP1 (note arrowheads), whereas the gust front (temperature break) and the onset of disturbance PP2 increasingly lagged behind PP1.* Four traces are shown in this figure because this evolution can essentially be described as a four-stage process.

1) Stage 1 (CXY): disturbance PP2 is characterized as a strong pressure increase;[2] is associated with a sudden drop in surface temperature and a rise in the dewpoint temperature; and follows a pronounced windshift, the appearance of gusty winds, and overcast, low cloud cover—all of which occur in conjunction with passage of the gust front. Meanwhile, PP1 is just beginning to emerge as an identifiable feature from the leading edge of the rapid pressure jump defining PP2. (Since it is not clear which of the two relative pressure maxima in the hour following 0000 UTC represents PP1, given that their temporal separation is smaller than can be well resolved by the barograph, the average of the two times is taken for the time of the relative maximum defining PP1.) There is some evidence to suggest a windshift associated with PP1, as CXY reports a shift from light southwesterlies to moderate west-northwesterlies coincidentally with passage of PP1, which is at least 30 min prior to the sudden temperature break and gust surge attributed to the gust front passage.

2) Stage 2 (PHL): this pressure trace shows that disturbance PP2 has weakened considerably from 2.1 mb at CXY to only 1.0 mb here. By contrast, PP1 is much more discernible. Corresponding loss in amplitude appears in the temperature, dewpoint temperature, and windspeed changes accompanying PP2, though a strong windshift with gusty winds and a thunderstorm still accompany the gust front passage, similar to stage 1.

3) Stage 3 (BWI): further weakening of PP2 and its associated temperature and wind variations is evident.

[2] The disturbances occurred during the time of semidiurnal pressure rise, the effect of which is filtered out later (Figs. 11–12) by use of a bandpass filtering technique. The arrowheads depict onset of a disturbance as defined by the beginning of the most rapid pressure rise.

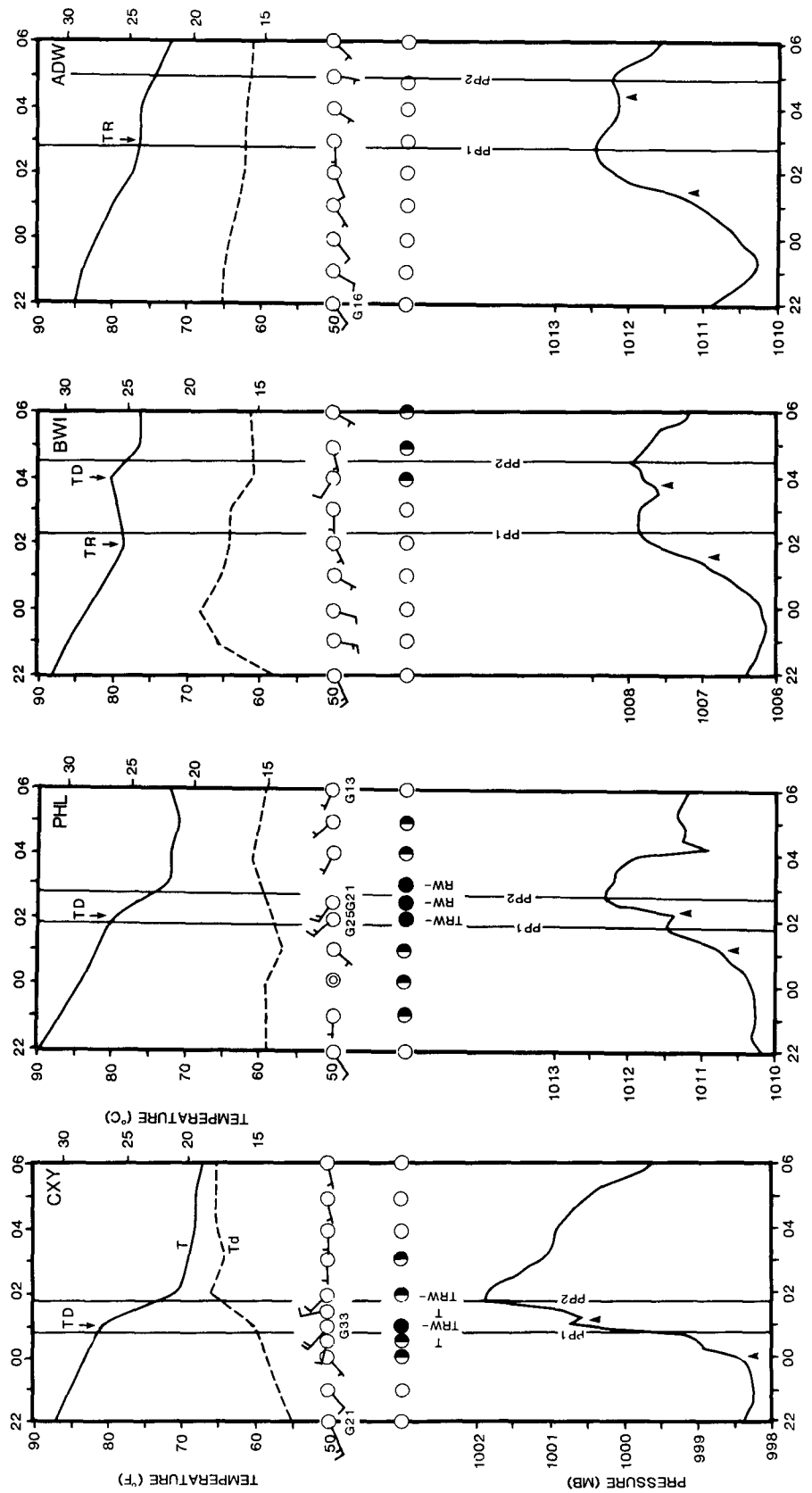

FIG. 6. Sample time traces from Harrisburg (CXY), Philadelphia (PHL), Baltimore (BWI), and Andrews Air Force Base (ADW) for the interval 2200 UTC 8 June–0600 UTC 9 June. Time series shown are for temperature T, dewpoint temperature T_d, and station pressure P. Sustained winds (barbs), wind gusts, low cloud cover (circles), and special observer remarks concerning precipitation are also shown. Hourly and "special" data were used for all variables except P, which utilizes 15-min interval digitized barograph data. Times of special events discussed in text are also denoted (PP1 = pressure perturbation 1, etc.) Arrowheads on pressure traces depict onset times for PP1 and PP2 (see text). Hourly estimated times of temperature drop associated with passage of thunderstorm outflow boundary denoted by "TD." Similarly, "TR" denotes times of temperature rise associated with bore-like disturbance PP1.

A significant strengthening of PP1 can now be discerned from 0.7 mb at PHL to 1.0 mb at BWI. The magnitude of PP1 is now greater than that of PP2 (0.6 mb). Thunder is no longer associated with the gust front, though it is still accompanied by the appearance of scattered low clouds, consistent with the nearby aerosol scattering ratio record at 0400 (Fig. 1b). These clouds are probably the remnant of the "arc cloud" typically found at the head of a gust front. The temporal separation between PP1 and PP2 has increased significantly to 2 h, allowing for easier discernment of the two windshifts associated with the two disturbances; note that the windshift accompanying PP2 is increasingly transient, as the winds stay northwesterly for perhaps only one hour. It is also important that surface temperature actually increases 2°C with the passage of PP1, a significantly different behavior than in the earlier stages.

4) Stage 4 (ADW): disturbance PP2 is by now barely discernible, being masked by the presence of the stronger disturbance PP1. Neither temperature changes, a wind discontinuity, nor the presence of low clouds are any longer evident with passage of PP2. Disturbance PP1 has reached its maximum amplitude of 1.3 mb. A gradual windshift still accompanies passage of PP1, but the temperature rise noted earlier is nearly absent.

2) Motion of the disturbances

Isochrone analyses of the gust front (temperature drop line) and associated disturbances PP1 and PP2 are depicted in Fig. 7. All three features dissipated in the Delmarva region; i.e., soon after arriving at the lidar site. It is also apparent that the gust front and its associated mesohigh feature PP2 originated in northwestern Pennsylvania and propagated south-southeastwards with similar speed, whereas PP1 formed later in the life cycle of the convective system in southern Pennsylvania and propagated much faster than the other features. A closer examination reveals that PP1 originated very close to the location of the gust front just prior to 0100, and then proceeded to outpace both it and PP2. Notice also that the rate at which PP1 outpaced the other features quickened after 0300, as the gust front and PP2 decelerated just prior to their demise.

A time–space cross section was constructed of the passage of the crests of disturbances PP1 and PP2 at stations within ~100 km of a line oriented nearly perpendicular to the direction of propagation of these phenomena (along line A–B in Fig. 5). Allowance was made for the fact that the isochrones were not truly straight lines. Thus, the position of each station in the cross section (Fig. 8) is the result of extending a line tangent to the local isochrones near that station to the plane of the cross section. It is apparent that PP1 develops later than PP2 and proceeds to propagate at a much faster speed, particularly after the deceleration of PP2 around 0300. Speeds of propagation prior to this time computed from the lines of regression in the diagram are 12.0 ± 2.5 m s^{-1} for PP2 and 22.8 ± 3.9 m s^{-1} for PP1.

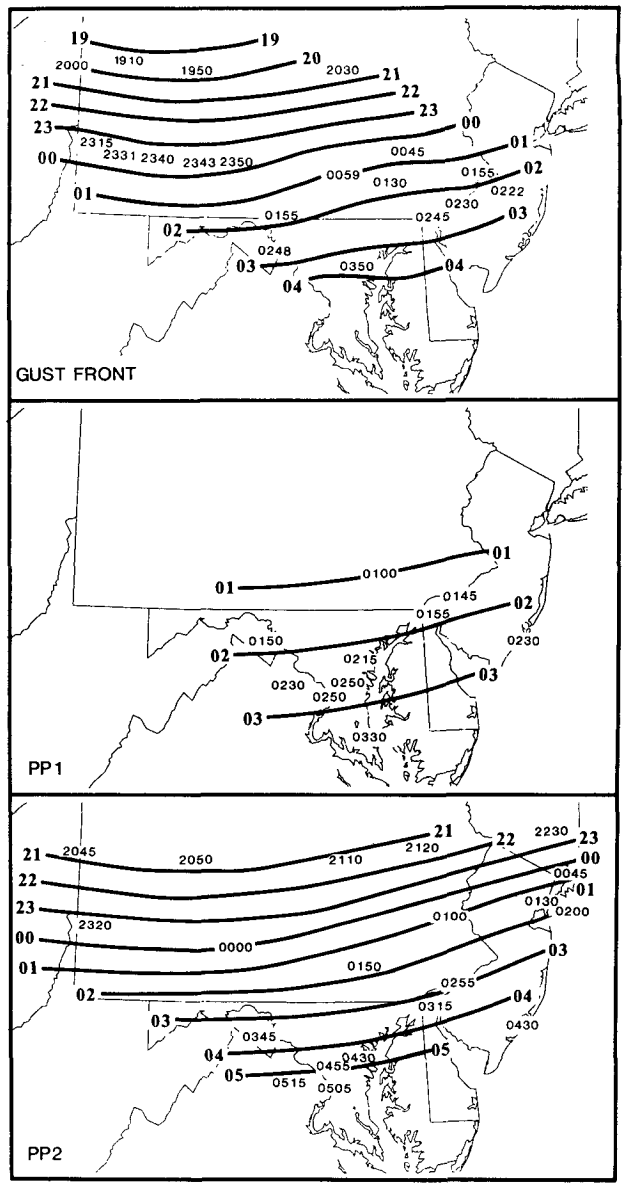

FIG. 7. Isochrones depicting passage of the gust front (temperature drop) and events PP1 and PP2. Times for these events denote when the maximum positive pressure perturbations associated with PP1 and PP2 occurred. Station locations are at the center of the 4-digit times.

3) Origin of the disturbances

The analyses presented so far strongly suggest that disturbance PP2 is a mesohigh hydrostatically related to the cold outflow from the squall line, and that the outflow (and associated pressure disturbance PP2) bears a striking resemblance to a gravity current.

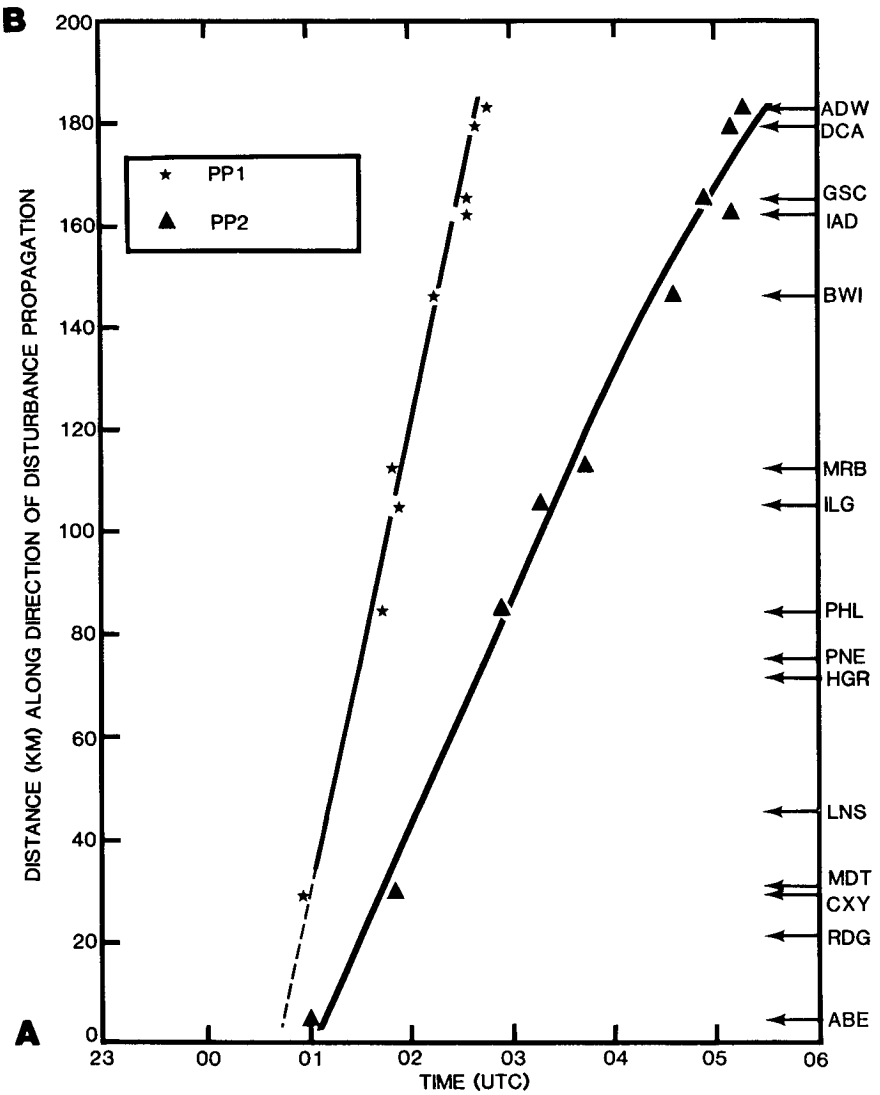

FIG. 8. Times of occurrence of significant events PP1 and PP2 at stations within ~100 km of a line oriented in the direction of their movement (Fig. 5). Line of regression fits to data appear prior to deceleration of PP2 (near MRB); their slopes give the speeds of propagation mentioned in text.

Thunderstorm cold outflows and their associated mesohighs have commonly been characterized as gravity current flows in the literature (e.g., Goff 1976; Wakimoto 1982; Simpson 1987). This hypothesis is given additional support by the observation that the rapid weakening of PP2 is highly correlated with the noted deceleration of the gust front in central Maryland, since the propagation speed of a gravity current is proportional to the square root of the hydrostatic pressure deviation (this is discussed later). Demonstration of this correlation appears in Fig. 9, which is a map of the pressure deviation amplitudes (p^*) ascribed to PP1 and PP2. The p^* values were subjectively determined as the absolute magnitude of pressure difference over the period of most rapid pressure change. Orientation of the isolines of equal p^* amplitude was constrained by the appearance of the squall line from infrared satellite imagery (Fig. 3), the surface analyses (Fig. 4), and the isochrone analyses (Fig. 7). This analysis shows that the greatest amplitude attained by PP2 of ~3.5 mb occurred in west-central Pennsylvania 3–4 h after the formation of the squall line. This disturbance rapidly weakened as it propagated into Maryland, being an order of magnitude less intense by the time it reached the lidar site six hours later. Contrastingly, disturbance PP1 seems to have originated near the leading edge of the cold outflow (Fig. 7) just as PP2 was rapidly weakening (Fig. 9), and subsequently intensified to a magnitude of nearly 2 mb by the time it entered Maryland. *This relationship between the two disturbances*

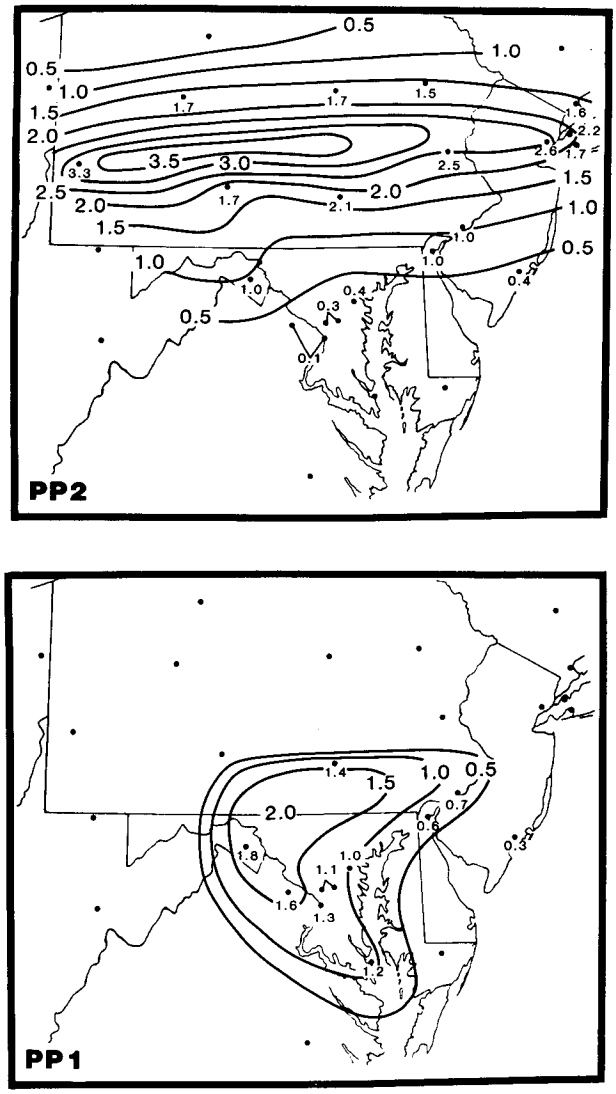

FIG. 9. Pressure deviation p^* amplitudes (mb) of pressure events PP1 and PP2 as derived from unfiltered barograph traces. Orientation of isolines was constrained by the appearance of squall line in satellite imagery (Fig. 3), the surface weather map analyses (Fig. 4), and the pressure perturbation isochrones (Fig. 7).

suggests that PP1 was generated at the leading edge of the cold outflow/gravity current system and grew at the expense of the dissipating gravity current.

Additional support for this idea is provided in the bandpass-filtered barograph traces shown in Fig. 11 across the mid-Atlantic area and in Fig. 12 for stations in central Maryland near the lidar site. These traces were produced with the Lanczos filter (Duchon 1979) shown in Fig. 10. This high-fidelity bandpass filter was devised to eliminate all periods except those similar to the ~1–3 h separation between PP1 and PP2 seen in the barograph display at GSFC and nearby stations (see Figs. 1a, 6, and 8). Inspection of Figs. 11 and 12 reveals that peak-to-trough amplitudes of the bandpass-filtered pressure perturbations (p') are only 50%–100% of the respective p^* amplitudes (Fig. 9), depending upon the period separating the two disturbances. Though the most representative estimate of the amplitudes of PP1 and PP2 is given by the p^* values, this method is not well suited for accurate definition of the times of occurrence of these events. Since the bandpass method is more objective than the p^* method, the nodal points in the p' time series will henceforth supply the onset times for each disturbance.

The resulting analyses clearly depict the weakening and demise of PP2 as it propagated south-southeastwards from the AOO–CXY–ABE region to the BWI–DCA region. Conversely, PP1 is possibly first evident as a minor pulse at CXY (either the weak "blip" on the trace at 0030 or that at 0100, neither of which can be resolved by the filter), becomes a pronounced event by the time it reaches MRB and PHL, and then rapidly intensifies to become stronger than PP2 by the time it has reached the Maryland network (Fig. 12).

It is concluded from this set of analyses (Figs. 6–12) that PP1 originated from the gravity current and its associated pressure disturbance (PP2). *Furthermore, the available evidence suggests that PP1 is an internal bore generated by the weakening gravity current,* in part because the temperature did not decrease with passage of this disturbance, but actually rose in a manner consistent with a bore (Fig. 6), in which surface warming may occur from downward mixing of potentially warmer air from above the low-level inversion (Shreffler and Binkowski 1981; Fulton et al. 1990). In ad-

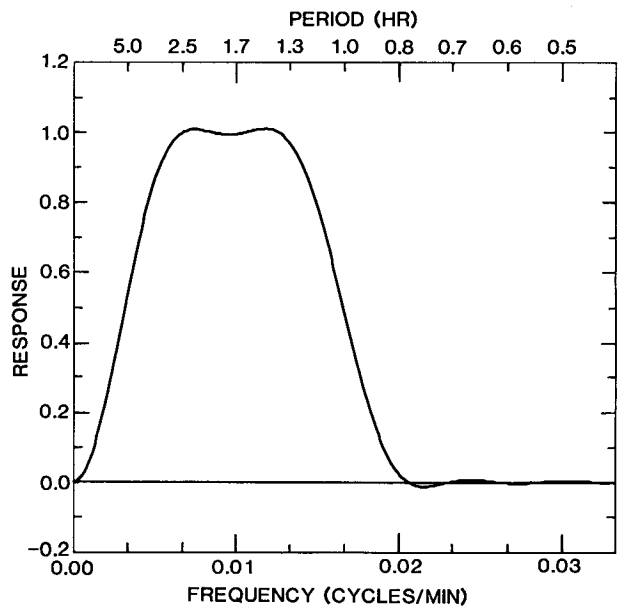

FIG. 10. Response function for the bandpass filter used in the analysis of the pressure time series data shown in Figs. 11 and 12. Filter selectively removes at least 50% of the amplitudes of disturbances with periods smaller than 1 h or larger than 5 h. Nyquist frequency is 0.033 min^{-1} for 15-min data.

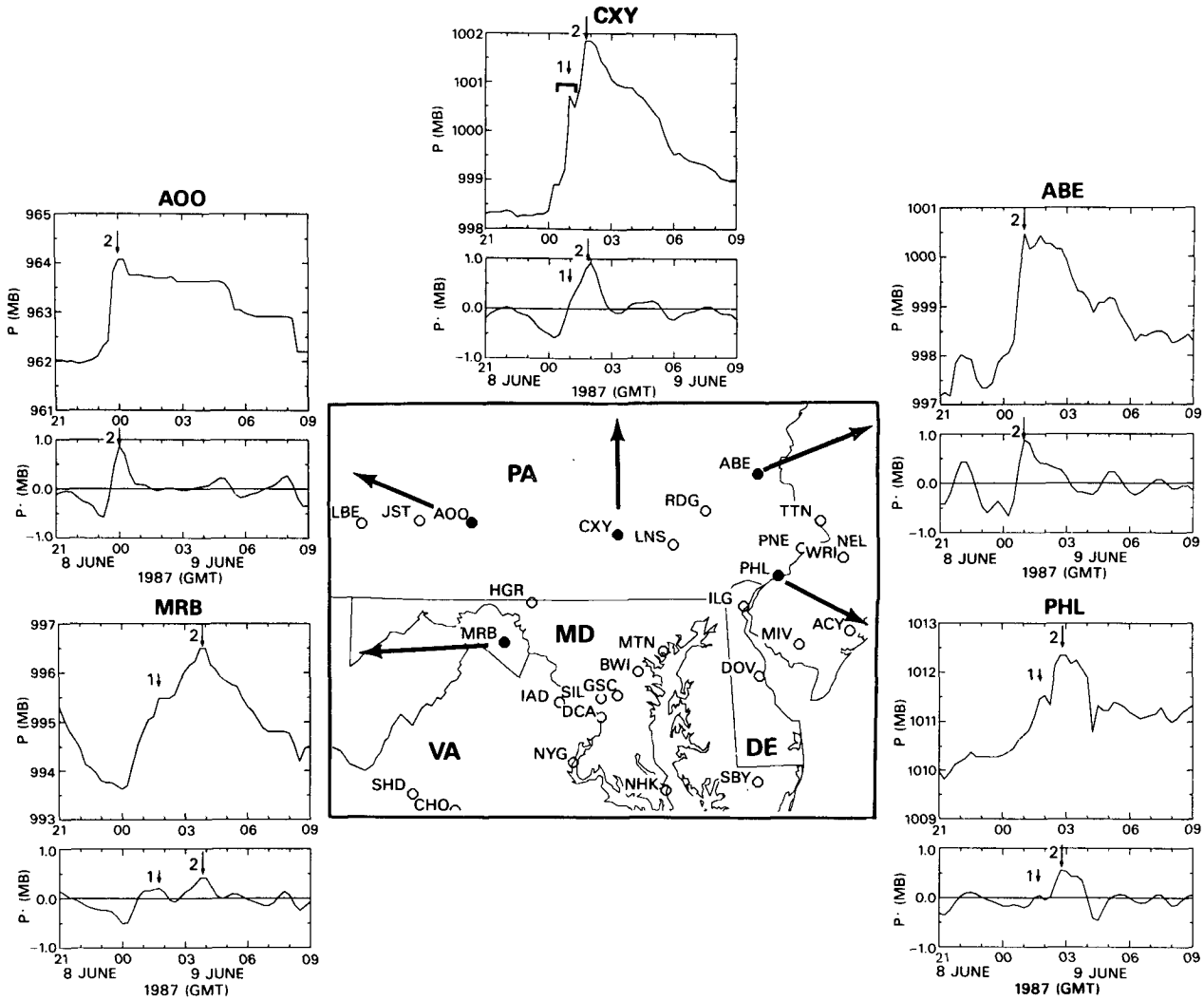

FIG. 11. Digitized barograph traces and their bandpass-filtered equivalents (p') from selected stations. This figure depicts evolution of pressure events PP1 and PP2 (denoted by 1 and 2 in traces) within mid-Atlantic area.

dition, a bore interpretation is consistent with the observations of a wind shift into the direction toward which the disturbance was propagating as it passed the stations, as well as the fact that the elevation of pressure following the initial jump associated with PP1 was either sustained or fell by less than 0.5 mb in all of the affected pressure traces [similar to the barograph displays for bores presented by Marks (1974) and others]. Of course, bores and gravity currents may display quite similar wind and surface barograph signatures, but their passage is not associated with similar surface temperature variations (Smith 1988; Fulton et al. 1990).

The AOO trace in Fig. 11 is a classic signature of a gravity current associated with a thunderstorm outflow: a sudden pressure jump, followed by a period of sustained pressure lasting for a few hours, and ending with a gradual tapering off of the mesohigh pressure to conditions similar to the initial state [in some cases pronounced "wake lows" can appear after the mesohigh has formed (Fujita 1963; Koch and McCarthy 1982)]. *Notice that the elevated pressure following PP2 is sustained—a feature that is only present at stations like AOO that did not experience the presence of PP1. This elevated pressure is almost entirely lost by the time the bore is just emerging somewhere in the area between CXY, ABE, and PHL. We interpret this fact as evidence that, as the gravity current weakened and PP1 developed, the pressure increase could no longer be sustained because of the transfer of energy to the developing bore,* similar in nature to the behavior of bore/gravity current systems observed in the laboratory (Maxworthy 1980). This progression can easily be followed by comparing the traces at AOO, CXY, and PHL in Fig. 11. Observe the decreased duration of the elevated pressure associated with PP2 as the bore-like disturbance PP1 develops.

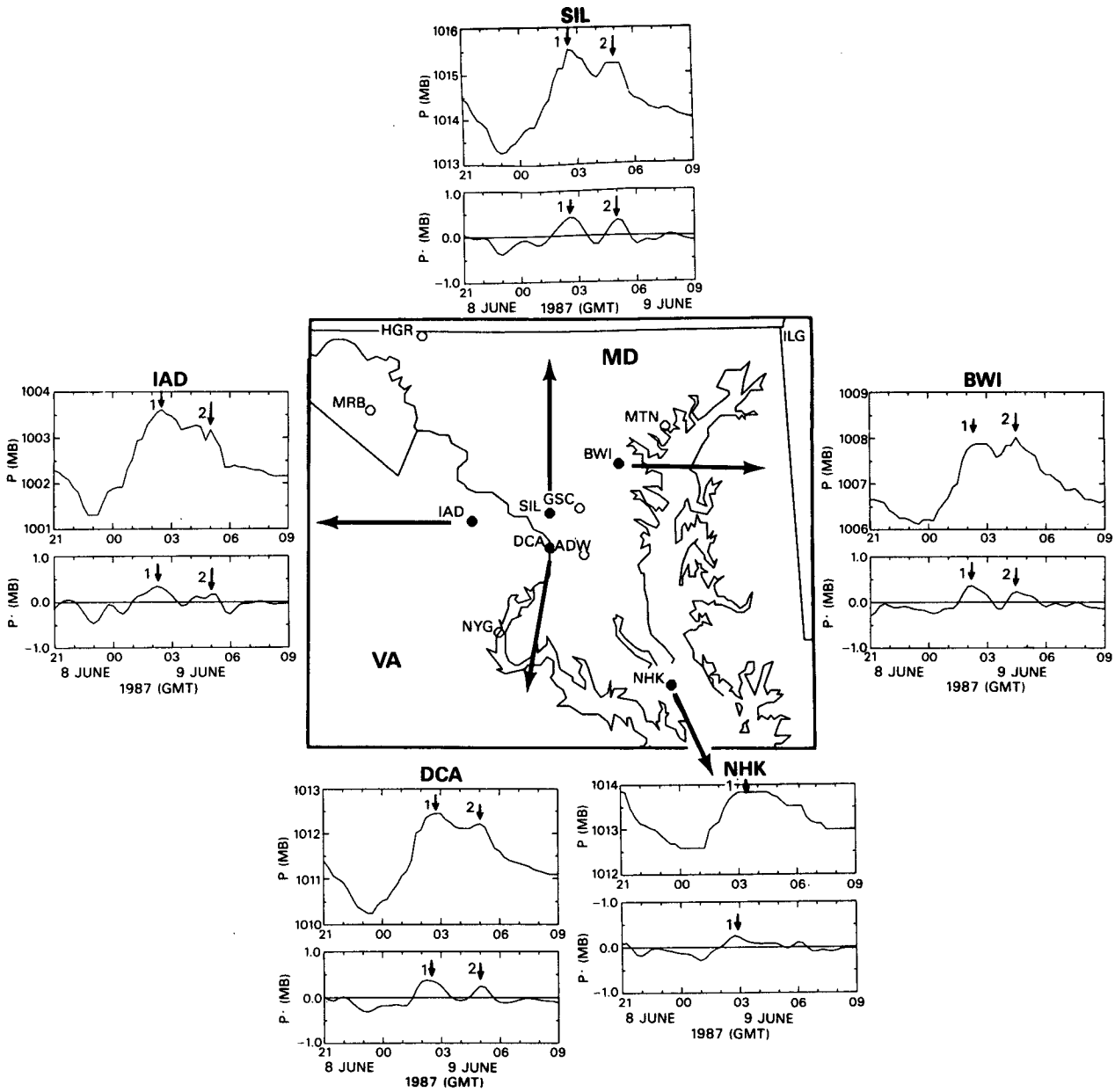

FIG. 12. As in Fig. 11, except for local sites in central Maryland.

c. Rawinsonde analyses

The rawinsonde data collected at the lidar site are extremely useful for a number of purposes. First, comparisons are drawn between the vertical profiles of moisture measured by the lidar and the rawinsondes to show the consistency between the two sets of measurements. Second, the moisture and temperature data from the rawinsondes are studied in light of what is known about PP1 and PP2 to assist in understanding their effects on the local atmosphere. Third, and most importantly, a synthesis of the rawinsonde and lidar data is performed to deduce the thermal structure of the disturbances.

Since the GSFC rawinsondes were released at 2252 UTC 8 June and at 0144, 0449, and 0752 UTC 9 June, whereas the lidar data collection covered the period 0144–0900, all but the first of these datasets can be compared with the lidar profiles (Fig. 13). Clearly the overall moisture structure measured by the two systems is in very good agreement, at least above the lowest 400 m where the laser and telescope are not fully aligned, and at relative humidities above 20%. Melfi and Whiteman (1985) and Melfi et al. (1989) discuss

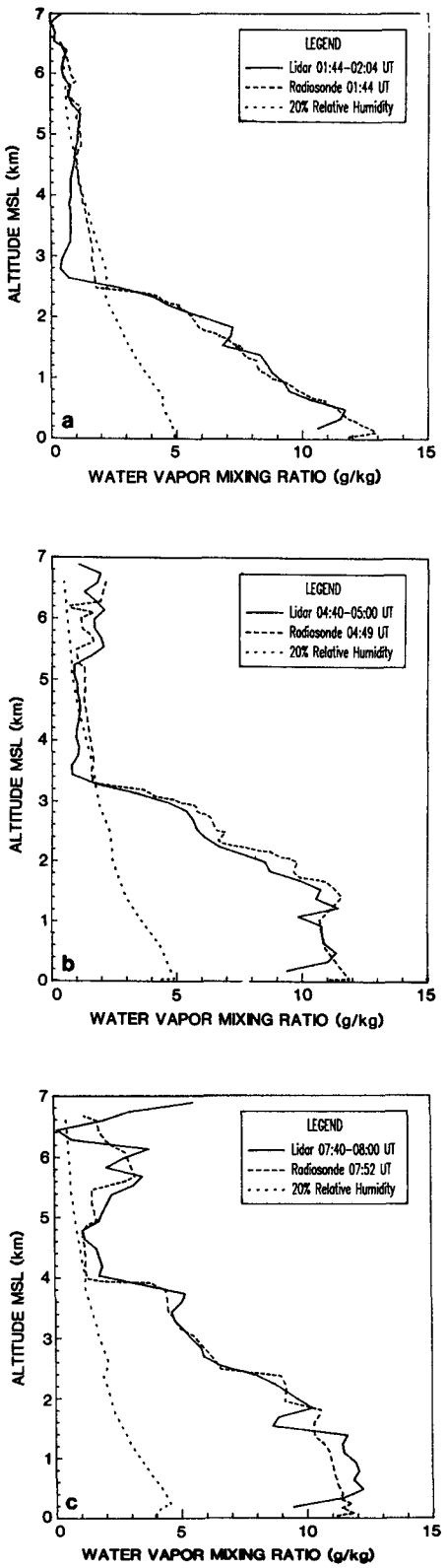

FIG. 13. Comparisons of lidar-derived profiles of water-vapor mixing ratio with collocated radiosonde measured profiles at 0144, 0449, and 0752 UTC 9 June 1987. Lidar profiles are averages over approximately ±10-min periods surrounding radiosonde releases.

the reasons for the failure of the rawinsonde to measure low relative humidities, whereas the lidar is sensitive to such moisture variations.

The 0144 sounding is believed representative of the prebore conditions for the following reasons. Recall that the time of onset of the pressure disturbances was defined as the beginning of positive pressure perturbation p', namely 0145 for PP1 and 0400 for PP2 (Fig. 12). These times are the same as the times of minima in relative pressure p^* appearing in Fig. 1a. Though the arrival of the "bore front" at 0145 as defined in the pressure trace is 30–45 min earlier than that deduced from the variation of the 10 g kg^{-1} mixing ratio surface (Fig. 1a), most of this difference can be explained by the sampling errors for the pressure data. In fact, the arrival of the gravity current front at 0400 is in excellent agreement with the time deduced from the lidar display.

Accordingly, the stratified moisture structure at 0144 is representative of the ambient atmosphere just before passage of the disturbance.[3] The lidar and rawinsonde data both show that the water vapor mixing ratio at 0144 decreases essentially linearly with height up to 2.4 km, and that this layer is capped by a 100–200 m layer of very rapid moisture decrease. Dramatic changes occur in the moisture profile by the time of the subsequent sounding at 0449, which was released after the passage of the gravity current front.

1) Substantial moistening has taken place throughout most of the atmosphere below 3.2 km; i.e., the former 2.4-km deep moist layer has increased in depth to this new height.

2) The lidar data show a considerable increase in moisture variability in the 1.0–1.8 km layer.

These changes are not short-lived and are even further augmented by 0752, as the moist layer deepens even more and increased variability is evident in the 1.0–1.8 km layer. *Furthermore, the 0.6–1.7 km layer has become essentially well mixed following passage of the mesoscale disturbances, in complete contrast to the earlier stratified structure.*

Profiles of mixing ratio and potential temperature measured by the rawinsondes at 0144 and 0449 are contrasted in Fig. 14 to emphasize the effects of the disturbances on the mesoscale atmosphere near the lidar site. As just mentioned, a large amount of moistening in the 0.6–3.2 km layer has resulted from passage of the disturbances. Thermal effects of the disturbances consist of the following developments.

1) Approximately 1°–2°C of cooling has occurred in the lowest 2 km.

[3] The earlier sounding at 2252 could be substituted just as well for this purpose, but the 0144 sounding is used here and in other analyses because of its closer proximity to the time of passage of the bore front.

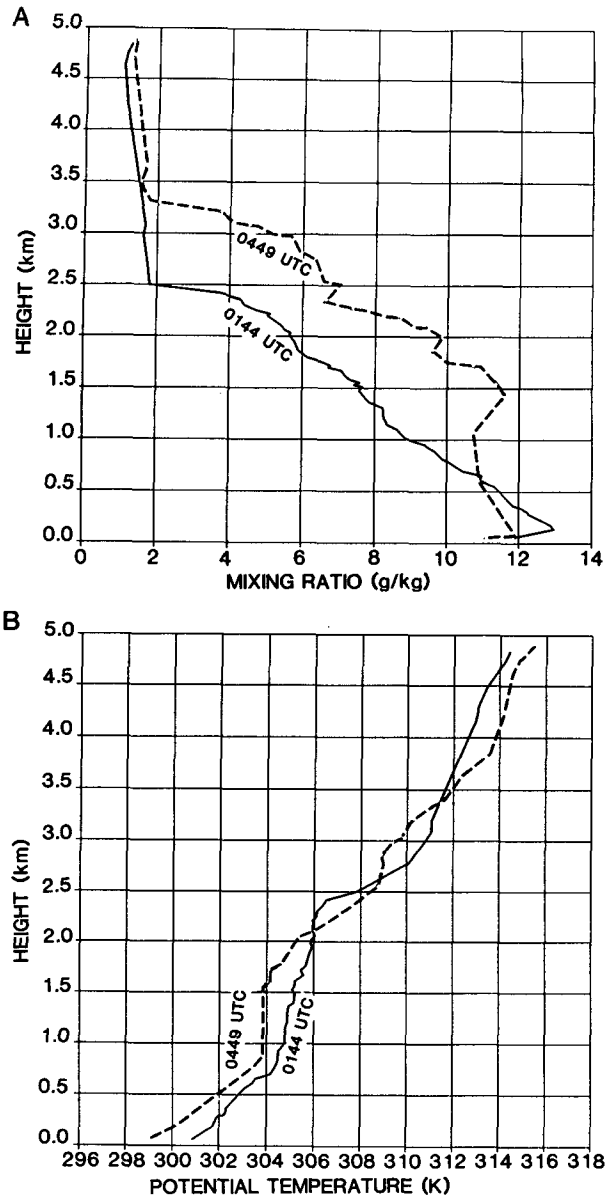

FIG. 14. Radiosonde-derived profiles of mixing ratio (top) and potential temperature (bottom) prior to bore passage (at 0144 UTC, solid lines) and subsequent to bore and gravity current passages (at 0449 UTC, dashed lines).

2) An elevated mixed layer in the 0.9–1.7 km altitude range develops as a combined consequence of the *apparent* maintenance of a surface-based stable layer and descent of the moisture-capping inversion previously at 2.4 km to 1.7 km. The height of the new elevated mixed layer corresponds well with the 0.6–1.7 km layer of increased mixing seen in the lidar moisture display.

Since the consistency between the lidar and rawinsonde moisture profiles has thus been established, it is reasonable to use the rawinsonde temperature data in conjunction with the detailed temporal information in the lidar moisture data to deduce the thermal structure of disturbances PP1 and PP2. Accordingly, a time–height cross-section analysis of virtual potential temperature (θ_v) was conducted (Fig. 15) in such a manner that the isentropes were constrained to be consistent both with the temperature soundings and the lidar-observed moisture structure. This was accomplished by first identifying each isentrope with a specific value of mixing ratio at the 0144 sounding release time, since that approximated the beginning of lidar data collection. Height variations of the isentropes between the sounding times then followed the lidar moisture observations in order to produce details concerning the effects of the disturbances. In other words, mixing ratio was used as a tracer for the mass (θ_v) fields, assuming that evaporation and condensation effects below 6 km were rather inconsequential for this period of time. This assumption is believed justified since the analysis period occurred during early evening and negligible, low cloud cover developed. A check on this assumption can be made by comparing the heights of the 306 and 310 K isentropic surfaces (thick lines) at the 0449 and 0752 sounding release times with the dashed lines, which represent the height variations of the moisture surfaces found to best approximate those θ_v values at 0144 (namely, the 10 and 3 g kg^{-1} mixing ratio surfaces—see Fig. 1a). The assumption seems to be quite good overall, with the largest discrepancy being ~0.3 km for the 310 K surface at the 0449 release time. A similar procedure was followed in the analysis of radiosonde data by Melfi et al. (1989) in their Raman lidar study of cold and warm fronts.

This data synthesis suggests that the 700-m deep stable layer existing at 0144 was *not* maintained intact, as suggested above; rather, it was totally disrupted upon passage of the bore front shortly thereafter. Coincidentally, an even stronger inversion was created at nearly the same height by the gravity current at 0400 with its associated low-level cooling effects (~2°–3°C), consistent with the BWI temperature record in Fig. 6. The first disturbance displays a behavior expected of an internal bore propagating on a surface-based inversion: it causes strong uplifting of this inversion surface and a net cooling in the lower troposphere of ~2°C with no perceptible cooling (in fact, slight warming) at the surface. This behavior resembles that seen in bore–gravity current studies that have utilized instrumented towers, which can sample the thermal structure of the disturbances at much higher sampling rates (e.g., Marks 1974). The bore-like disturbance exerts an indirect influence on the atmosphere as high as the overlying inversion originally at the 2.5-km level, wherein the disturbance amplitude is severely damped. *Notice that the well-mixed region in the 0.9–1.7 km layer at 0449 discussed above is actually a by-product of the bore and resides above the stably stratified air contained within the gravity current.* The depth of this elevated mixed region gradually increases, but becomes less well defined thereafter in a manner consistent with the moisture profiles in Fig. 13. It is important to bear in mind

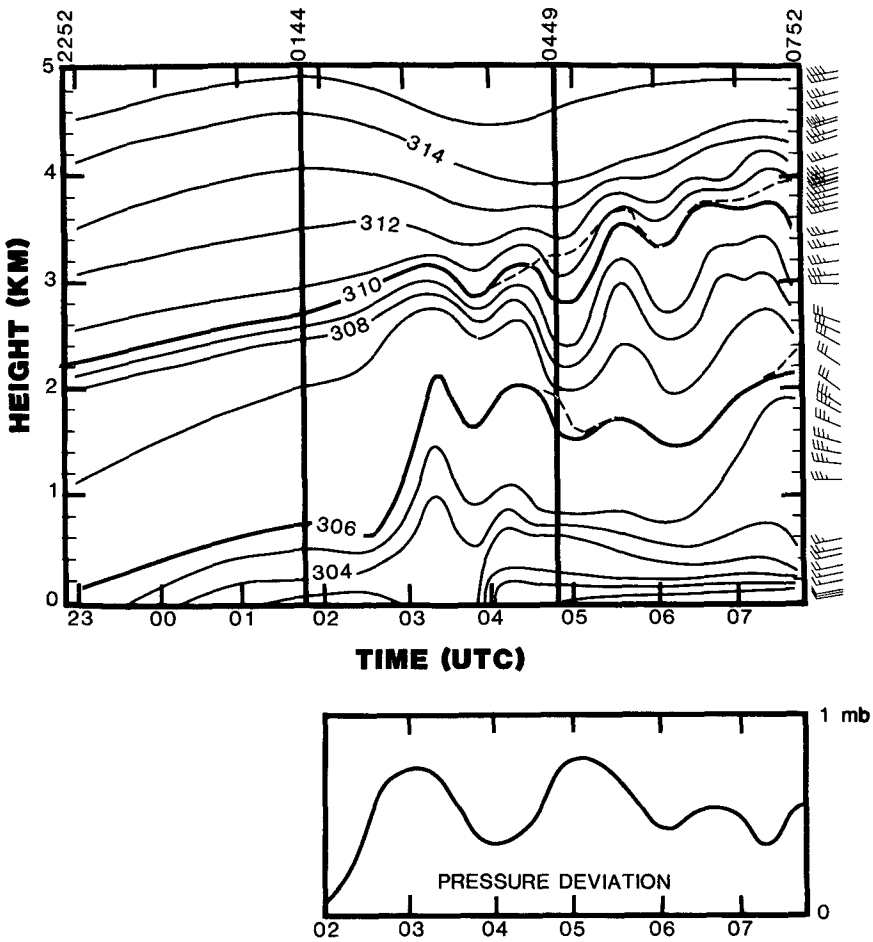

FIG. 15. Time–height cross section of virtual potential temperature (K) at the lidar site. Isentropes are drawn to be consistent with both the four radiosondes launched on 8–9 June 1987 at designated times (vertical bars) and the lidar-observed moisture structure with temporal scales larger than one hour (compare to Fig. 1a). For example, temporal variations in the heights of the 306 and 310 K isentropes (thick lines) are given by variations in the heights of the 10 and 3 g kg^{-1} mixing ratio surfaces, respectively. Dashed lines near the time of radiosonde releases denote lidar-observed variation of moisture surfaces that deviate from assumed variations. Winds were only available from the 0752 UTC rawinsonde release. Barograph trace shown beneath cross section is identical to that appearing in Fig. 1, and depicts the p^* variation for comparison with the isentropic variations.

that all of these details are in keeping with the moisture variations seen in the lidar display. Furthermore, there is generally good agreement between the isentropic (mass) variations associated with the bore and gravity current and the collocated pressure trace (reproduced in Fig. 15 from Fig. 1), at least within the acceptable range of difference of ±15–30 min dictated by the barograph sampling interval. Notice, in particular, the general agreement between the times at which pressure began rising with the appearance of the two disturbances (at 0200 and 0400) and the onset of isentropic layer upliftings (at 0230 and 0400).

In summary, the observations presented thus far are strongly suggestive that the two major disturbances seen in the lidar and barograph data are an internal bore and a dissipating gravity current, the latter of which apparently generated the bore as it weakened and collapsed into the developing nocturnal inversion layer. This interpretation is subjected to more rigorous comparison with theory, which appears in the next section.

5. Comparisons with theory

Here we attempt to draw comparisons between the observations and the theoretical predictions concerning certain properties of gravity currents and bores for the purpose of providing additional support for this interpretation of the Raman lidar data. An excellent review of observational, theoretical, laboratory, and numerical treatments of gravity currents, bores, and related phenomena is provided by Simpson (1987). Other useful summaries pertaining primarily to bores and solitary

waves are given in Christie et al. (1978, 1979) and Smith (1988).

a. Disturbance PP2: A dissipating gravity current?

The hypothesis that disturbance PP2 is a manifestation of a weakening gravity current can be given much greater support if it can be demonstrated that

1) the depth of a gravity current predicted hydrostatically from the observed surface temperature and pressure changes near the lidar site is comparable to that deduced from the lidar observations;
2) the speed of propagation of PP2 prior to its deceleration is consistent with that predicted from gravity current theory with the given set of observations;
3) there exists a region of positive "feeder" flow behind the leading edge of the gravity current; i.e., relative flow directed toward the head of the current. Unfortunately, our observations are inadequate to employ this test because no wind data was obtained from the crucial rawinsonde release at 0449 (Fig. 15).

An equation for the mean depth of a gravity current d_o can be derived from application of the hydrostatic assumption, by further assuming that the density difference between the cold and warm air masses does not vary with height, and that the current does not produce significant buoyancy variations in the ambient atmosphere. The derivation given in the Appendix shows d_o can thereby be expressed simply in terms of surface variables as

$$d_o = \frac{T_{vc}\Delta p}{\rho_w g\,[(p_c/p_w)T_{vw} - T_{vc}]} \qquad (1)$$

where g is gravitational acceleration; T_v (K) is the virtual temperature; subscripts c and w refer to the cold and warm air masses behind and ahead of the leading edge of the gravity current, respectively; $\Delta p = p_c - p_w$ is the pressure difference associated with its passage; and ρ_w is the density of the warm air mass. Our analysis utilizes the surface temperature data at Baltimore (BWI) and the average of the Δp values at BWI, SIL, and GSC (Fig. 5), since these stations are near or at the lidar site. It is necessary to perform this calculation locally, rather than further upstream when the outflow/gravity current system was younger, since the depth decreases with increasing distance from the source of the cold outflow.

The extreme sensitivity of the current depth calculations to the various assumptions mentioned above has been discussed by Smith and Reeder (1988). A particularly acute problem with application of the theory to observations is that the actual temperature difference between the two air masses ΔT is usually a function both of height and the distance behind the leading edge of the gravity current. Fortunately, the gust front passed BWI just before the hour (at 0350 according to Fig. 7), and as demonstrated below from the lidar–radiosonde data synthesis (Fig. 18), the conditions one hour following the passage of the gravity current front represent quite well the mean properties of the cold current. The hourly surface data at BWI suggest that the surface temperature variation across the gravity current is $\Delta T = 2.5 \pm 1$°C (Fig. 6), whereas the average of the local barograph records gives $\Delta p = p_c - p_w = 0.5 \pm 0.1$ mb (Fig. 12). On the other hand, we have no knowledge of the variation of the density (potential temperature) difference throughout the depth of the gravity current. A crude estimate can be made by assuming a linear decrease of density difference with height throughout the depth of the gravity current to a zero value at $z = d_o$. Substitution into (1) of the resulting vertical mean of $\Delta T = 1.3$°C, in the manner suggested by Smith and Reeder (1988), together with $\Delta p = 0.5$ mb, results in a predicted gravity current depth of $d_o = 0.9 \pm 0.5$ km. Although the error bounds on this predicted value are quite large, the mean value is a reasonable one for an atmospheric gravity current. More importantly, it agrees quite well with the *mean* depth of stably stratified air that underlies the well-mixed layer *immediately* following passage of the head of the gravity current-like disturbance (Fig. 15). Therefore, this value of $d_o = 0.9$ km will be used in the additional theoretical analyses to follow.

The next question concerns the consistency between the observed and predicted velocities of propagation for PP2 *prior to its deceleration.* An expression for the speed of propagation C_{gc} of a gravity current relative to the upstream wind, which is consistent with the expression (1) for the current depth, is given by (Carbone et al. 1982; Simpson 1987)

$$C_{gc} = F_d\left\{gd_o\left[\frac{(p_c/p_w)T_{vw} - T_{vc}}{T_{vc}}\right]\right\}^{0.5} \qquad (2)$$

where F_d is the appropriate Froude number. This expression is not only plagued by the same uncertainties in ΔT as above, but is compounded by the problem of needing an appropriate value for d_o and the Froude number as well. Most of these difficulties can be avoided by assuming that the observed Δp value is purely a hydrostatic consequence of cooling associated with passage of the gravity current, whereupon an alternate expression for its speed of propagation, which utilizes only surface barograph data and requires no direct knowledge of the current depth, can be derived from (1) and (2) as (e.g., Wakimoto 1982; Seitter 1983)

$$C_{gc} = F_d(\Delta p/\rho_w)^{1/2}. \qquad (3)$$

Thus, in terms of parameter value uncertainties, the only significant ones remaining in the gravity current speed equation are the pressure difference and the Froude number. Care is taken to ensure that nonhydrostatic effects on the pressure change, which would likely be important only near the head of the current, are minimized by considering only pressures away from the head region. The observations at Harrisburg (CXY) and neighboring stations AOO and ABE (Fig. 11) are

used in a manner similar to that described earlier for the calculations of the current depth at the lidar site, resulting in $\Delta p = 2.1 \pm 0.4$ mb. Choosing an appropriate value for the Froude number is more of a problem. Laboratory and numerical experiments indicate that F_d can take on a value anywhere from 0.75 to 1.41 (Simpson 1987; Smith and Reeder 1988). The largest of these values ($2^{1/2}$) is appropriate only for a steady flow in an inviscid, unstratified, infinitely deep fluid, and is an unlikely value for atmospheric gravity currents in which the effects of mixing and surface friction are important. A more appropriate range of values is probably $F_d \sim 0.8$–1.1 when d_o is taken to be the mean depth of the cold air (e.g., Carbone 1982; Koch 1984). This range of Froude numbers yields the prediction $C_{gc} = 13.0 \pm 3.2$ m s^{-1}, compared to the observed value of 12.0 m s^{-1} prior to deceleration of the current. *Thus, the predicted speed of the gravity current agrees with that characterizing the motion of PP2 within the observational uncertainties.*

The presence of a tail or head wind will alter this prediction significantly and also influences the shape and speed of the gravity current (Simpson 1987); however, these effects can be ignored in the present environment (actually shown later, cf. Fig. 17). It is also important to realize that these gravity current formulas rest upon certain assumptions, including a steady current moving into an unstratified atmosphere containing no vertical wind shear. The present situation is characterized by a dissipating (nonsteady) system moving into an increasingly stratified atmosphere containing substantial vertical wind shear in the lowest 3 km. However, the nonsteady nature of the situation should not be of great consequence, since the comparison of the observations with theoretical prediction of the gravity current speed takes place prior to the deceleration/dissipation of the system (at CXY at 0100 UTC). Furthermore, the special GSFC soundings show that stratification in the lower troposphere was minor prior to the development of the surface-based stable layer, though stratification above 2.5-km altitude existed at that time. Thus, some uncertainties arguably remain, but they are unlikely to create such a problem for the present case as to make any comparisons with the theory pointless or meaningless. Besides, some estimate of both the depth and motion of the gravity current at the time of bore genesis is needed for the analysis of the bore properties discussed next; it is our belief that it is preferable to have some theoretical justification for performing such an analysis to simply using the observed speed of motion and the lidar-derived depth measured hours later in such an analysis.

It is concluded that the following evidence suggests disturbance PP2 to be a dissipating gravity current.

1) The disturbance is a mesohigh produced by cold outflow from a dissipating squall line.

2) The rate of propagation of PP2 and the gust front/temperature drop are quite similar.

3) Gust front deceleration occurred simultaneously with the rapid loss in pressure amplitude of PP2; i.e., with increasing distance from the cold air source.

4) The pressure excess is hydrostatically consistent with the outflow depth deduced from the lidar–rawinsonde synthesized observations.

5) The observed propagation speed prior to the deceleration of PP2 is consistent with that predicted by steady-state gravity current theory.

b. Disturbance PP1: An internal bore?

The hypothesis that disturbance PP1 is an internal bore generated by the collapse of the gravity current can be given much greater support if it can be demonstrated that

1) this disturbance attains a depth and propagates at a speed consistent with that of a bore of at least moderate intensity; and

2) the predicted bore depth is comparable to that derived from the observations.

Atmospheric bores are typically generated by gravity currents in the presence of pronounced static stability at and near the surface (Rottman and Simpson 1989). According to Simpson (1987), the character of the bore depends on the ratio of its mean depth to that of the stable layer in the warm air (h_l/h_o): smooth undular bores are observed in the laboratory for $1 < h_l/h_o < 2$, whereas increased mixing, due to shear instability, occurs for $2 < h_l/h_o < 4$; and for even larger values, the bore appears more like a gravity current. In all cases, the flow of the air within the stable layer is partially blocked by the gravity current, acting similarly to a solid obstacle to the flow. A bore thus generated will move forward along the stable layer following its development as a smooth hump enveloping the head of the gravity current. Eventually, the bore leaves behind the dense air associated with the parent gravity current.

Prediction of bore properties from the known environmental structure can be made from either simple two-layer hydraulic theory or a numerical model utilizing the primitive equations. An example of the latter approach is the anelastic, nonhydrostatic model of Haase and Smith (1989a) containing variable eddy diffusivity, a sophisticated numerical advection scheme, and a stretched vertical grid. This rather complex model was used by Haase and Smith (1989b) to study the evolution of a gravity current as it encountered a surface-based stable layer capped by a deep neutral layer, conditions highly conducive to the generation of undular bores. Unfortunately, one of the two basic parameters governing the evolution of their gravity current-bore system is a Froude number that is a function of the "inflow velocity" characterizing the cold feeder flow; but our data are not sufficient to prescribe such a value with sufficient accuracy. Since by comparison the governing parameters for hydraulic theory can be

estimated relatively accurately with the available data, we choose to employ it instead for our purposes.

According to hydraulic theory, four types of disturbance can be forced by a gravity current as it encounters a surface-based stable layer (Rottman and Simpson 1989), as depicted in Fig. 16. The actual type is seen to be a function both of the nondimensional depth (d_o/h_o) and speed (F_h) of the gravity current, where

$$F_h = \frac{C_{gc}}{C_{gw}}, \tag{4}$$

C_{gc} is the speed of the steady-state gravity current (relative to the medium), and C_{gw} is the phase speed of a long, internal gravity wave formed at the inversion interface capping the surface-based stable layer in an atmosphere containing no vertical wind shear (Simpson 1987; Smith 1988). This speed is given in terms of the depth (h_o) and strength ($\Delta\theta_v$) of the inversion occurring in the air ahead of the bore according to

$$C_{gw} = (g'h_o)^{1/2} = \left[g\left(\frac{\Delta\theta_v}{\theta_v}\right)h_o\right]^{1/2}. \tag{5}$$

The stable layer in the air just ahead of the bore-like disturbance was previously determined to have a depth of h_o = 0.7 km (Fig. 14). A 0.7% density difference ($\Delta\theta_v$ = 2 K) across the inversion is calculated upon assuming a linear increase of θ_v with height in the stable layer. Use of these values and the previous estimate for C_{gc} from (3) results in a Froude number F_h = 13.0/6.8 = 1.9.

The other parameter required to predict the bore properties is the nondimensional current depth (d_o/h_o), which requires an estimate prior to the deceleration of the gravity current and near the time when the bore was generated. Use of the surface conditions near Harrisburg at 0100 UTC [Δp = 2.1 mb from Fig. 12 and ΔT = (5.7 ± 1°C)/2 from Fig. 6] results in a predicted current depth of d_o = 1.7 ± 0.5 km, which is nearly

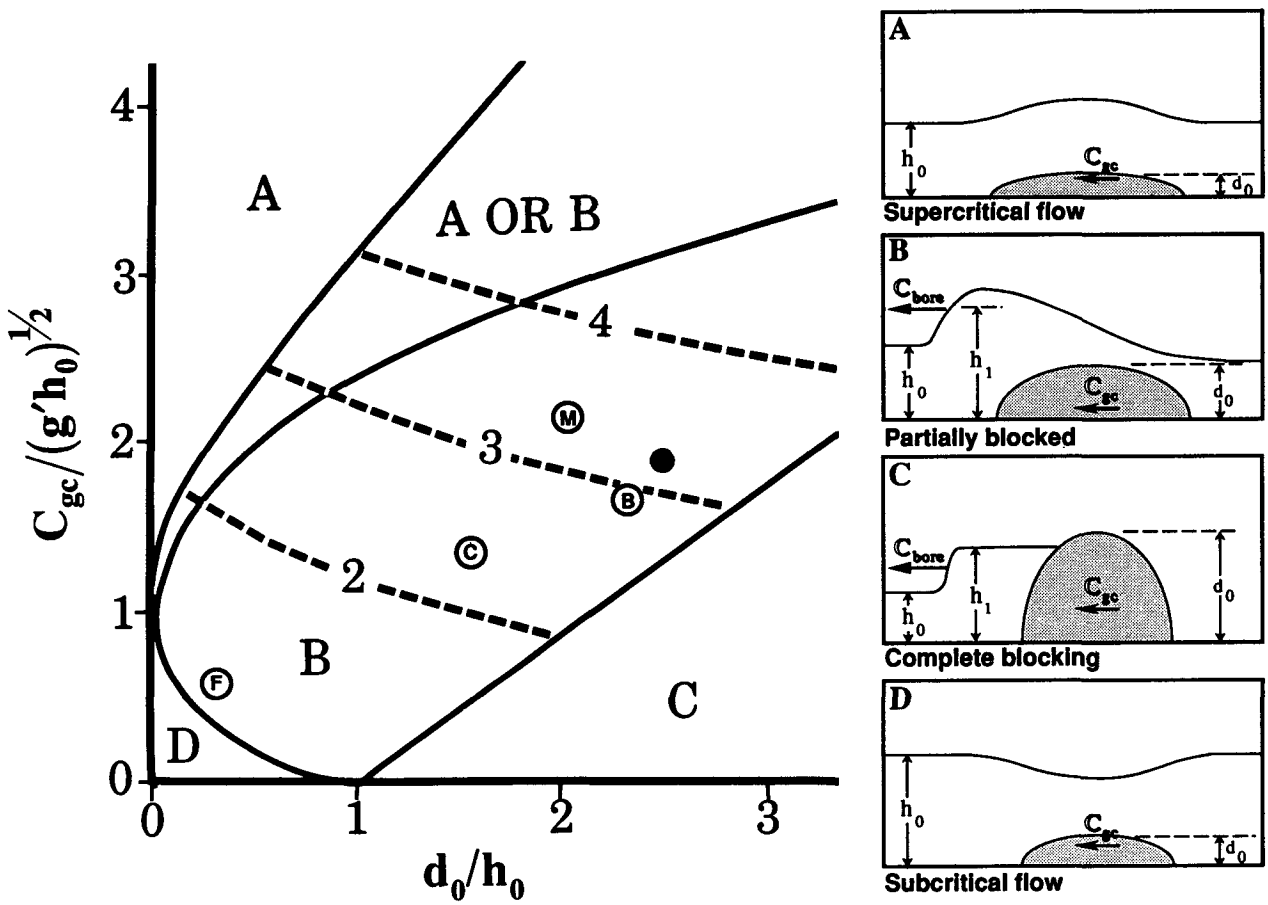

FIG. 16. Strength (h_l/h_o) of internal bores (dashed lines) generated by gravity currents with nondimensionalized speed [$C_{gc}/(g'h_o)^{1/2}$] and depth (d_o/h_o), as described by two-layer hydraulic theory (Rottman and Simpson 1989). Bore depth is given by h_l. Four types of disturbance can be generated at the interface h_o between two fluids of differing density by a gravity current (shaded obstacle) propagating at speed C_{gc}, but bores (elevated interface) are generated only in cases B and C depicting at least partial blocking. (After Simpson 1987). Dot denotes bore of strength ~ 2.7 estimated from the data analysis in the present study. Circled values are measurements derived from other observational studies of thunderstorm-generated bores: B, Bedard and Saunders (1978); C, Carbone et al. (1990); F, Fulton et al. (1990); and M, Marks (1974).

twice that previously calculated at the lidar site at 0400. This difference reflects the likelihood that the current was much stronger and deeper at the earlier time. Although there is no way to verify this prediction, as was done at the later time against the lidar observations, it is assumed that it is reasonably accurate, in view of the good agreement with the observations at the later time. To the extent that this is true, $d_o/h_o = 1.7/0.7 = 2.4$ results.

These Froude number and nondimensional current depth values predict an internal undular bore of strength $h_l/h_o = 3.2$ (see solid dot in Fig. 16), from which we conclude that the bore would have a mean depth of $h_l = 2.2$ km. Of course, the error bounds on the predicted bore strength are relatively large, due primarily to the previously discussed uncertainties in the appropriate values for d_o and C_{gc}. Nevertheless, *this prediction of the bore depth is in excellent agreement with the lidar observations* (Fig. 1a) showing dramatic lifting of the inversion (associated with the 10 g kg^{-1} surface) to a maximum (mean) height of 2.1 (1.9) km at 0315.

The remaining question concerns the bore speed, which hydraulic theory predicts to be a function of its strength and C_{gw} (Rottman and Simpson 1989) as given by

$$\frac{C_{\text{bore}}}{C_{gw}} = \left[\frac{1}{2}\left(\frac{h_l}{h_o}\right)\left(1 + \frac{h_l}{h_o}\right)\right]^{1/2}. \tag{6}$$

This expression predicts a bore speed of 17.6 m s^{-1} upon substituting the predicted bore strength value of 3.2. Use of the observed strength thus gives a predicted speed that is in fairly good agreement (±20%) with that determined from the barographs (22.8 m s^{-1}).

In summary, the favorable comparisons between these theoretical calculations and the observations of the bore mean depth and speed of propagation provide further support for the hypothesis that disturbance PP1 is an internal undular bore generated in some manner by the dissipating gravity current. These results are based on the simple two-layer hydraulic model of Rottman and Simpson (1989), which neglects nonhydrostatic effects, as well as the effects of moisture, wind shear, and the vertical leakage of wave energy that may occur in a continuously stratified environment.

At least some of these effects can be addressed. Crook (1986) has suggested that moisture reduces the amplitude of the bore. However, we are not compelled to consider further these effects since they are minor.

Wind shear effects have not previously been introduced into theoretical studies of bores, with the exception of its influence on wave trapping by Crook (1988). Bores cannot be maintained for very long in the absence of some means to trap the upward leakage of wave energy that occurs in a stratified atmosphere. (Incidentally, the existence of strong wave trapping adds some justification to our attempt to compare the bore depth observed by the lidar with that calculated upstream hours earlier when the bore was just developing from the leading edge of the gravity current.) Effective wave trapping has been shown by Crook (1988) to be possible when any of the following conditions are met: (i) winds in the middle and upper troposphere oppose bore motion, or (ii) a midtropospheric inversion is found at a specific height above the lower stable layer, or (iii) an opposing jet with considerable curvature exists in the lower troposphere.

The effectiveness of these various mechanisms in the present case was investigated with the only GSFC sounding that contained wind data (0752 UTC 9 June—see Fig. 15), as well as with the nearest National Weather Service sounding [the 0000 UTC 9 June sounding taken at Dulles (IAD)—see Fig. 5]. The advantages of the GSFC sounding are that its vertical resolution is nearly triple that of the Dulles sounding in the lower troposphere, and that it was launched precisely at the lidar site. Its chief disadvantage is that the GSFC launch occurred 5 h after bore passage; thus, it contains a more stably stratified layer near the ground (resulting from both radiational cooling and the gravity current) than that which characterized the prebore environment. Analyses for both soundings are shown in Fig. 17 for intercomparison.

Profiles of the wind component in the direction of wave propagation (U) shown in Figs. 17a,d for the two soundings exhibit strong relative flow opposing the bore motion [$(U - C_{\text{bore}}) < 0$] in the lowest 5 km of the atmosphere. However, this relative flow decreases to zero values aloft (not shown), so the opposing upper-level wind mechanism of Crook cannot act as a wave trapping mechanism here.

Likewise, though the existence of the midtropospheric inversion at the 2.5-km level (still present in a weakened state at 0752—see Fig. 15) may seem to suggest the possibility that Crook's second trapping mechanism might have operated, more detailed analysis indicates this could not have been the case. In particular, the greatest reduction of upward energy propagation occurs when the weakly stratified region separating this inversion from the surface-based stable layer is exactly one quarter of a vertical wavelength deep; i.e., when this region has a depth equaling $\pi/2m$, where m is the vertical wavenumber given by

$$m^2 = \frac{N^2}{(U - C)^2} - \frac{U''}{U - C} - k^2 \tag{7}$$

from the Taylor–Goldstein equation, and $N^2 = [(g/\theta_v)\partial\theta_v/\partial z]$ is the Brunt–Väisälä frequency, $U'' = \partial^2 U/\partial z^2$, and $k = 2\pi/\lambda$ is the horizontal wavenumber. The Scorer parameter $l^2 = m^2 + k^2$ is identical with m^2 when k^2 is negligible, as it is here. An estimate for l^2 is greatly complicated by the fact that its sign shifts

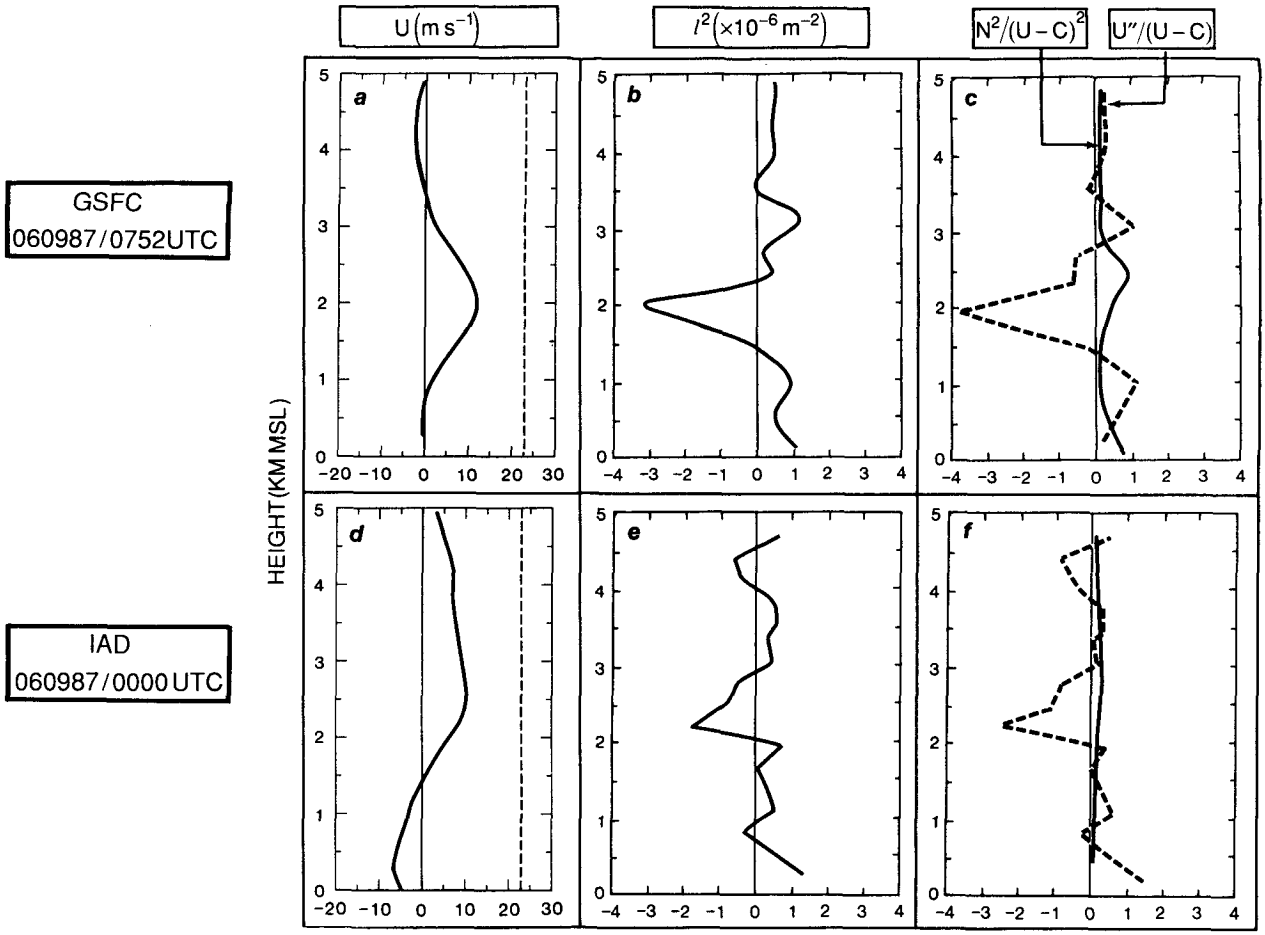

FIG. 17. Analysis of ability of local atmosphere to trap bore energy. Shown are vertical profiles of: (a) wind component in the direction of bore propagation (solid curve, m s^{-1}) and bore speed (dashed line); (b) square of the Scorer parameter (l^2, 10^{-6} m^{-2}); and (c) contributing terms in the expression for l^2 (10^{-6} m^{-2}). These profiles were calculated from the 0752 9 June 1987 special sounding released at the GSFC lidar site, whereas panels (d)–(f) depict profiles of the same parameters calculated from the 0000 UTC 9 June 1987 Dulles synoptic sounding.

from positive to negative within the weakly stratified region from 0.9 to 1.7 km (see Fig. 17b). Use of an average absolute value for $l = m = 7.8 \times 10^{-4}$ m^{-1} in the weakly stratified layer existing above the surface-based layer (Fig. 14) results in a requirement for this layer to be 2.0 km deep for effective wave trapping; but this is considerably deeper than the actual layer depth of 0.8 km, so this does not appear to be an effective wave trapping mechanism.

In fact, the most plausible mechanism for effectively trapping the upward propagation of wave energy is the opposing low-level jet. Comparison of the vertical profiles of the first two terms in (7) shows that the curvature term dominates the profile of l^2 (Figs. 17c,f). Curvature in the wind profile is the important element here, since the $U''/(U - C)$ term in (7) increases the Scorer parameter in the lowest levels and reduces it above the jet level where the curvature is strongly negative. The resultant decrease of l^2 with height to strongly negative values at the ~2.1-km level in both soundings—even though separated in time by nearly 8 h—attests to the persistence of a strong wave trapping mechanism.

Existence of this mechanism is important for several reasons. First, it affects the bore properties in ways perhaps not accounted for properly by the two-layer theory (though vertical leakage of wave energy is also ignored by the theory). Second, it offers a plausible explanation for the observed sustenance of the bore for at least 2.5 h (Fig. 7). Third, the Scorer parameter profiles suggest that atmospheric perturbations produced by the bore should have diminished rapidly with increasing height near the 2.1-km level and that, consistent with the suppression of wave vertical energy propagation, no significant tilt should be displayed by those isentropes that were perturbed by the bore. It is seen in Fig. 15 that these predictions agree exceedingly well with the observations. *This additional consistency between the observations and theory not only provides greater support for the bore hypothesis but further attests to the*

validity of details appearing in the Raman lidar measurements.

It is concluded that disturbance PP1 displays the character of an internal undular bore, for the following reasons.

1) The disturbance is accompanied by a windshift into the direction of bore movement, a sudden jump in pressure that is sustained for 2–3 h, and a net cooling in the lower atmosphere without any cooling at the surface (in fact, warming occurred as is often observed with bores).

2) Generation of the disturbance occurred coincidentally with rapid weakening of the gravity current at the leading edge of the gust front, suggesting the gravity current to be its source.

3) The constant rate of propagation of PP1 is consistent with that of a bore, in contradistinction to the dissipating gravity current, which it outpaces.

4) The disturbance occurs in an atmosphere that contains a pronounced surface-based inversion, required for bore existence; air within this layer is rapidly lifted by the disturbance almost to the level of a midtropospheric inversion.

5) Two-layer hydraulic theory predicts the disturbance to be an internal undular bore given the observed speed of disturbance PP1, the estimated depth of the gravity current, and the local atmospheric structure.

6) Prediction of an effective wave trapping mechanism at the 2.1-km level is in excellent agreement with the observed behavior of the disturbance as seen in the lidar data.

7) Finally, the predicted bore depth of 2.2 km is entirely consistent with the lidar display.

c. *Synthesis of the observations and theory*

The success of the comparisons between the theoretical predictions of the characteristics of gravity currents and bores and the observations pertaining to PP1 and PP2 brings us to the following conclusions, as summarized schematically in Fig. 18. Beginning at the left in this diagram, the first feature to appear is the ambient stable layer, whose depth h_o was estimated from the rawinsonde data to be 0.7 km (corresponding to the 10 g kg^{-1} mixing ratio surface). The depth of the moist air at this time was established as 2.5 km (corresponding approximately to the 3 g kg^{-1} surface), but grows to nearly 4 km by the end of the lidar data record at 0800 as a consequence of the passage of disturbances PP1 and PP2 and the resulting strong vertical mixing. The first disturbance displays the character of an internal bore propagating on the surface-based stable layer at 0300–0315. Its passage is obvious as a major uplifting of the surface-based inversion surface to an altitude of 2.1 km. The mean bore depth of h_l = 1.9 km is also shown. Perturbations in the streamlines indicate that effects of bore lifting are indirectly felt as high as the 3-km level. Thick haze or scattered fractocumulus clouds (wavy hatching) diagnosed in the aerosol backscattering ratio data appear to develop in response to this forced lifting of moist air, since they form near the time of peak upward displacement. The haze layer then descends in accordance with the descent of the height of the mixing ratio surfaces to a minimum following the passage of PP1. Assuming that mixing ratio surfaces act as tracers of the flow field in the absence of significant condensation or evaporation processes, and further assuming that the flow field can be adequately described by steady-state, two-dimensional processes in the plane of this cross section (the direction of propagation of the disturbances), then this descent is interpreted as an actual air parcel descent and hence explains the descent of the haze layer.

The scale of the bore "head" as estimated from its speed of propagation using the principle of time-to-space conversion (note scale at bottom of Fig. 18) is 30–40 km. Considerable mixing follows in the wake of the bore according to the lidar display, consistent with its predicted strength h_l/h_o = 3.2 (Simpson 1987). This elevated mixed region is constrained to the altitude range 0.9–1.7 km by the time of the rawinsonde release at 0449, in part because the atmosphere below 0.9 km is occupied by cooler air contained within the gravity current, which first appeared in the BWI surface observations at ~0400. The maximum depth attained by the gravity current is idealized to take place within its head (D_o) concurrently with the second peaking of the 10 g kg^{-1} surface at ~0430, in slight disagreement with the GSFC barograph trace indicating the peak pressure defining passage of PP2 at 0500. The streamlines indicate that air parcels experience renewed lifting with the passage of the gravity current. Thick haze or scattered low clouds are seen to reform in response to the renewed lifting. Even greater mixing accompanies the gravity current, and the depth of the moist layer grows accordingly.

d. *Comparisons with other observations*

It is of interest to compare these results to other observations of atmospheric internal bores apparently generated by thunderstorm gravity currents. Since the present study describes an internal undular bore that has not yet outlived its source gravity current, it falls into the category of "early bore" studies (Marks 1974; Bedard and Saunders 1978; Fulton et al. 1990; Carbone et al. 1990). Other studies have described solitary waves and/or bores that have already outlived their thunderstorm gravity current (Shreffler and Binkowski 1981; Haase and Smith 1984; Doviak and Ge 1984). This comparison is faciliated with use of Table 1, which shows findings determined from these studies. Related investigations of thunderstorm-generated gravity currents and possible bores—wherein useful measures of both bore depth (h_l) and inversion depth (h_o) were *not*

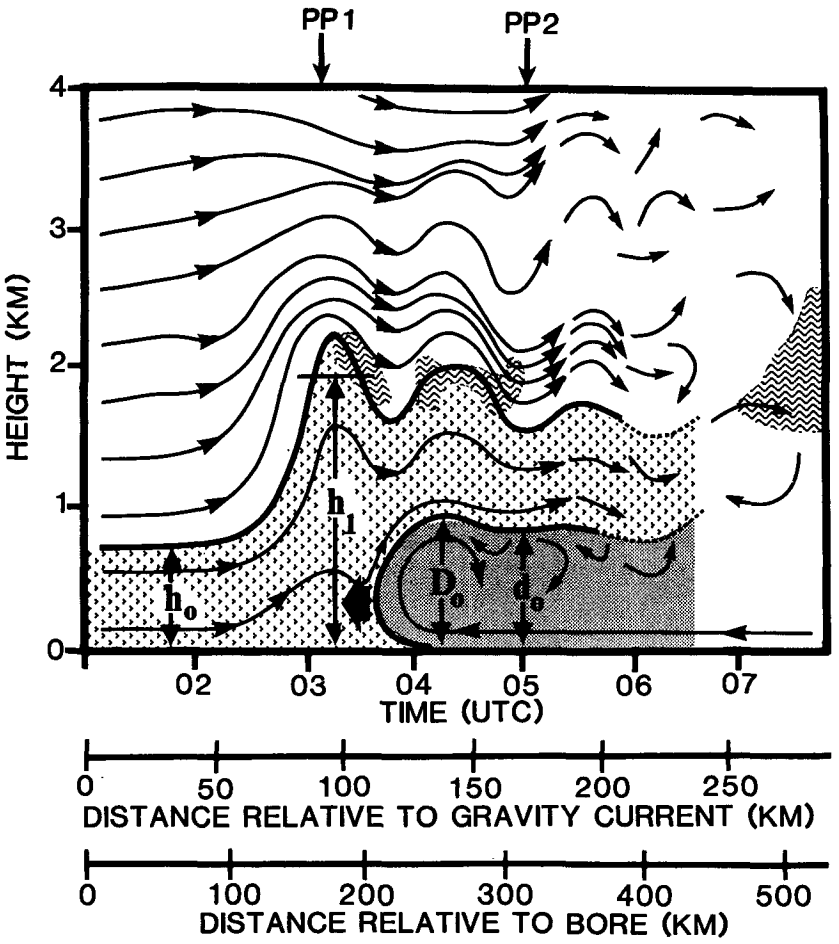

FIG. 18. Schematic diagram of the structure and airflow characterizing the internal bore (light stippling) and gravity current (dark shading) on 8–9 June 1987 as diagnosed from a synthesis of the lidar, barograph, surface, and rawinsonde data with theoretical predictions. Gravity current is shown propagating to the left (large arrow). Depths of gravity current (d_o), its head (D_o), the bore (h_l), and preexisting surface-based inversion (h_o) are shown. The air contained within the bore is defined by the 10 g kg^{-1} mixing ratio surface (upper thick curve) demarcating the low-level inversion. All streamlines follow directly from the isentropic analysis in Fig. 15 prior to 0600, and degenerate into turbulence thereafter as suggested by the diffuse nature that later characterizes the moisture structure (Fig. 1a). Streamlines are drawn to be consistent with moisture field (assuming mixing ratio acts as tracer of flow field) and laboratory studies of gravity currents and bores. Note the relationship between strong lifting at the leading edge of the bore and subsequent formation of thick haze or scattered cloud debris (wavey hatching) as derived from the aerosol scattering ratio (Fig. 1b).

reported [e.g., studies by Charba (1974) and Scott and Ackerman (1983)]—do not appear in this table.

It is apparent that the most reliable observations of h_l have been obtained in studies like the present one, in which lidars or acoustic sounders were employed (Marks 1974; Bedard and Saunders 1978; Shreffler and Binkowski 1981). On the other hand, a disadvantage of the present study is that the surface observations lacked sufficient temporal resolution to permit accurate estimates of the rate at which pressure and temperature changed with passage of the bore. In any case, at least the *magnitude* of these changes accompanying the 8–9 June 1987 bore—1.1-mb pressure increase and 2°C warming—compare well with other studies, since Table 1 shows that thunderstorm-generated bores/solitary waves seem to be characterized by a pressure jump of 1–6 mb and a slight (0°–3°C) temperature rise. The bore in the present study apparently propagated slightly faster than in any previously reported event, although uncertainty in our estimate of bore speed resulting from sparse data coverage in the area between the lidar site and the point of origin of the bore (Fig. 7) prevents us from drawing firm conclusions. More significantly, we find that both the predicted and lidar-observed mean

TABLE 1. Observed characteristics of internal undular bores/solitary waves generated by a thunderstorm gravity current.

Reference	Special sensor systems used	Opposing low-level jet?	Bore characteristics						
			$\partial P/\partial t$[a] (mb/min)	$\partial T/\partial t$[a] (°C/min)	C_{bore} (m s^{-1})	F_h	h_1[b] (km)	$\left(\frac{h_1}{h_0}\right)^b$	$\frac{d_0}{h_0}$
EARLY bore studies[c]									
Marks (1974)	acoustic sounder, 444-m tower								
Bedard and Saunders (1978)	acoustic sounder, radar, mesonet								
Fulton et al. (1990)[d]	444-m tower, Doppler radar,	?	1.1/9	?	6	2.2	0.4	2.3 (3.3)	2.0
	mesonet	?	?	?	13	1.7	0.8	2.3 (3.0)	2.3
Carbone et al. (1990)	Doppler radars, mesonet,	Yes	5.5/10	+0.5/7	22	>0.6	~1.1	>0.4 (>1)	>0.3
	special raobs	Yes	1.5/?	>0	18	1.3	(2.3)	(2.3)	1.5
8–9 June 1987 case	Raman lidar, special raobs	Yes	1.1/60	+2/60	23	1.9	1.9 (2.2)	2.7 (3.2)	2.4
MATURE bore studies[c]									
Shreffler and Binkowski (1981)	aerosol lidar, mesonet, special raobs								
Haase and Smith (1984)[d]	444-m tower, mesonet, special raobs	Yes	1.5/6	+3/10	13		1.8	1.8	
Doviak and Ge (1984)[d]	444-m tower, Doppler radar, mesonet	Yes	4.0/5	~0	17		~1.2	~0.9	
		Yes	1.3/17	~0	13		~1.0	~2.0	

[a] These local derivatives refer to the maximum pressure and temperature changes accompanying passage of the bore.

[b] Parenthetical values are those from two-layer theory (Simpson 1987; Rottman and Simpson 1989), whereas other values were directly observed.

[c] Early bore studies are those for which the parent gravity current could still be found in the observations, whereas mature bore studies describe bores and/or solitary waves after they have long since outlived their gravity current source.

[d] The bore depth in these studies was not known to better than ±50% accuracy, either because of the large vertical separation between the tower top and the lowest level of Doppler radar data or related problems. In addition, the inversion height (h_0) was not well known.

bore height (h_l), as well as the lidar-observed strength (h_l/h_o) observed in the 8–9 June case substantially exceed any previously measured or inferred values (in fact, quoted values are often the maximum bore heights). Notice, however, that this value for the bore strength falls well within the range of predicted values reported in most other studies. Comparison of our observations and predicted bore strength values with those in the other early bore studies also appears in Fig. 16.

The substantial mixing following the bore as inferred from the Raman lidar display is testimony to the observed strength of this bore. Precisely why this bore displayed such a strong character is unknown. However, the answer probably lies in some combination of factors, including (i) a strong cold-pool source for the thunderstorm gravity current (since the kinetic energy of the current, which indirectly determines the speed of the bore, depends on the cold-pool depth and strength); and (ii) the existence of a neutrally stratified layer above a shallow nocturnal inversion (since the inversion depth must be small relative to the depth of the gravity current). Recent numerical experiments by Haase and Smith (1989b) suggest that the bore/solitary wave becomes less undular in appearance and stronger in amplitude as the surface-based stable layer decreases in depth. These factors appear to be necessary, but may not be sufficient, to produce strong bores generated by thunderstorm gust fronts. In addition, the common existence of an opposing low-level jet seen in all studies in which wind profiles were presented (Table 1) suggests the strong possibility that this mechanism for trapping wave energy is a plausible explanation for the frequently observed long lifetimes of thunderstorm-generated bores.

6. On the relationship of cloud formation to bore strength

Returning momentarily to the schematic summary (Fig. 18), notice that most of the lifting accompanying bore passage occurs within a 30-min period beginning at 0245. The low-level inversion originally at the 0.7-km level has been lifted only ~100 m by then, but is subsequently forced at a much more rapid rate to the 2.1-km level by 0315. The computed mean vertical motion during this ~30-min period of rapid ascent is $w = 0.7$ m s^{-1}. It should be recalled that this estimate is based on the time-filtered lidar data (e.g., white curves in Fig. 1), which contain essentially no small-scale fluctuations. On the other hand, the unfiltered data exhibited transients near the beginning of this period of rapid ascent with intensities of 2–4 m s^{-1}. However, since such excursions do not represent the *net* effect of the bore disturbance on air parcels, the filtered dataset was used instead for these purposes.

An identical procedure was applied to the other material surfaces in Fig. 18 to estimate profiles of net parcel displacement and resultant vertical velocity induced by the bore. These profiles are depicted in the right panel of Fig. 19. Maximum vertical displacements of $\eta = 1.3$ km occur for parcels originally at a height of

$z = 0.8$ km, and diminish to negligible levels for parcels above 2.4 km. Notice that the most rapid falloff in $\eta(z)$ occurs just above 2 km, in accordance with the results of the wave trapping analysis.

Effects of bore passage on the thermal and moisture structure of the local atmosphere were determined by applying the $\eta(z)$ profile to the 0144 GSFC sounding (thick lines in left panel of Fig. 19), which is representative of the potentially unstable conditions just ahead of the bore front. The computed sounding resulting from this lifting (depicted by the light lines) exhibits the following effects directly caused by the bore:

1) The surface-based inversion layer in the lowest 0.7 km of the atmosphere is lifted to a height of 1.0–1.5 km and greatly weakened, in agreement with the isentropic cross-section analysis.

2) Likewise, the base of the midtropospheric inversion is weakened and lifted to 2.9 km from its earlier altitude of 2.5 km.

3) Considerable increase in relative humidity results as parcels conserve their mixing ratio during adiabatic ascent; although condensation of water vapor does not occur in the strictest sense, the resulting maximum of 83% found at the 2-km level is quite consistent with the formation of thick haze or fractocumulus clouds precisely at that level at the crest of the bore that was deduced from the lidar observations.

4) Despite the increased moistening and destabilization, and the weakening of the midtropospheric restraining inversion, this strong bore was still unable to force parcels to their levels of free convection because the amount of lifting at the height of this inversion was too weak to eliminate it.

These results indicate that strong lifting by the bore was confined to too shallow a layer near the surface to trigger deep convection. Alternatively, it might be reasoned that the *magnitude* of lifting was insufficient to trigger deep convection. In any case, the net vertical motion accompanying the bore as estimated from the Raman lidar data is believed reasonable, since it is similar to the ~ 1 m s^{-1} maximum value that can be *inferred* from the aerosol lidar display in the bore study by Shreffler and Binkowski (1981) and the 1.5 m s^{-1} value actually *measured* by a tall instrumented tower during sampling of a bore, as reported by Marks (1974). However, these values are much smaller than the 4–15 m s^{-1} peak upward velocities that have been determined with Doppler radar in the studies of Doviak and Ge (1984), Fulton et al. (1990), and Carbone et al. (1990), and the 3–5 m s^{-1} values associated with "morning-glory" bore-like phenomena as obtained from balloon, aircraft, and photogrammetric analysis of cloud motions by Clarke et al. (1981). Probably the

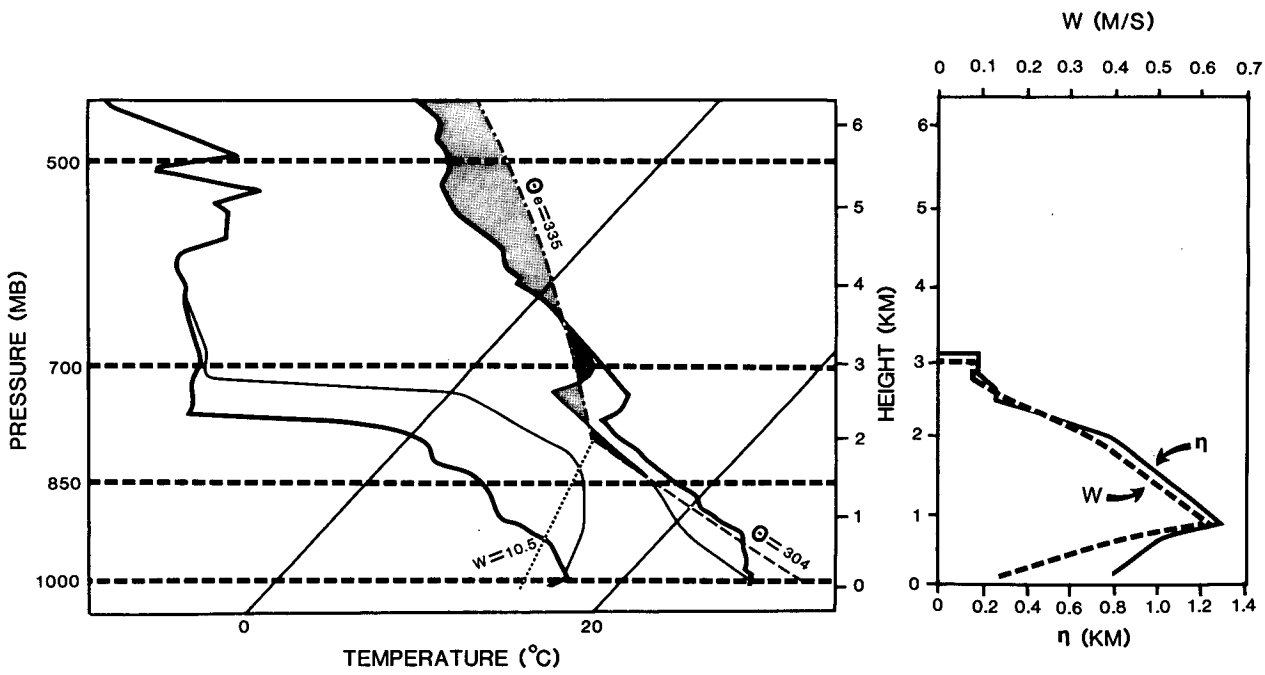

FIG. 19. Determination of the ability of observed bore to produce condensation in ambient atmosphere represented by the 0144 GSFC sounding (thick lines). The result of applying parcel displacement profile $\eta(z)$, shown in right panel (as obtained from Fig. 18), to this sounding is depicted by light lines. Lifting almost creates condensation at 2-km level; however, parcels still cannot freely attain their levels of free convection without imposing additional mechanical forcing (amount needed is depicted by areas of dark shading on resultant sounding defined by parcel path given by dash-dotted curve).

major reason for these differences is that the updrafts in these other studies were associated with bores whose characteristic horizontal scale is only a fraction of the ~35-km width of the bore head deduced in the present case. The different manner in which the vertical motions are obtained is also a consideration, since in most of these other studies, they are nearly instantaneous values, as opposed to the 30-min average used in the present case. In addition, Doppler radar analyses contain uncertainties due to the errors that accumulate during upward integration of the continuity equation, as well as other problems. These uncertainties can be large, such as in the case by Fulton et al. (1990) where estimates of the bore depth could not be obtained to an accuracy better than 50%. Of course, the lidar-derived motions are merely inferred values, and their validity also rests upon the imposition of various assumptions.

Despite these differences, the present study provides additional evidence to support findings from other studies that very strong forcing within a shallow boundary layer may not be sufficient to trigger deep convection. For example, no storms developed from bore forcing in the case of Fulton et al. (1990), even though 15 m s^{-1} upward velocities were estimated. It is interesting that Carbone et al. (1990) found that forcing by a gust front alone was not sufficient for this purpose, since it propagated for several hours without initiating storms, yet a squall line developed extremely rapidly out of virtually clear skies once the bore-like gust front simultaneously collided with a quasi-stationary dryline and a soliton-like disturbance. In addition to the increased lifting resulting from this collision process (as previously suggested in studies by Purdom 1982; Wilson and Schreiber 1986; etc.), Carbone's gust front also encountered enhanced moisture and a strong low-level jet, factors that were suggested to have produced more erect updrafts and less convective inhibition. Thus, the present study complements recent findings from these other studies, which suggest that the following considerations are important in determining the ability of gravity currents, bores, and large-amplitude solitary waves to trigger deep convection: (i) the strength of the low-level forcing, (ii) the depth of the low-level forcing relative to the height of the capping inversion, (iii) the strength of the capping inversion, (iv) the nature of the low-level wind shear, and (v) the moisture and potential instability present in the ambient atmosphere.

7. Conclusions

This paper has further demonstrated the ability of the Raman lidar to observe detailed vertical structures of mesoscale phenomena from profiles of water vapor mixing ratio and aerosol backscattering ratio. A careful synthesis of the lidar data with special rawinsonde data, as well as conventional surface and GOES satellite data, has permitted an assessment of the time–space continuity and dynamic nature of two boundary-layer disturbances seen in the high-resolution lidar data. Upon assuming that mixing ratio is a conserved variable in the absence of condensation and evaporation processes, a comparison of the lidar display with the rawinsonde data permitted determination of the thermal fields associated with these disturbances at extremely high temporal resolution (2 min) and to an altitude of 6 km, which greatly exceeded the depths of the disturbances. Furthermore, the airflow associated with the disturbances was inferred by synthesizing the lidar and rawinsonde data.

One of the two disturbances was shown to be a dissipating outflow boundary (gust front) spawned by an intense squall line several hours prior to its detection by the lidar. Comparison of the observations with theory strongly suggested that this disturbance could be characterized as a gravity current, in particular (i) the disturbance was a mesohigh produced by cold outflow from a dissipating squall line; (ii) its motion was quite similar to that of the gust front/temperature drop; (iii) gust front deceleration occurred simultaneously with the rapid loss in pressure amplitude of the disturbance, (iv) the pressure excess was shown to be hydrostatically consistent with the outflow depth deduced from the lidar-rawinsonde synthesized observations; and (v) the observed propagation speed fell well within the range of estimates predicted by gravity current theory.

The second disturbance observed in the Raman lidar data appears to have been an internal bore propagating ahead of the gravity current on a surface-based stable layer, which acted as a wave guide. The bore was generated coincidentally with rapid weakening and deceleration of the gravity current at the leading edge of the gust front, suggesting that it generated the bore. Its constant rate of propagation is in contradistinction to the dissipating gravity current, which it outpaced. Passage of the bore was marked by a net cooling in the lower troposphere hydrostatically consistent with the observed sudden jump in pressure, a slight warming at the surface, and a windshift into the direction of bore movement and was followed by a sustained elevated pressure. Comparisons between the observed and predicted depths and speeds of propagation of the bore offered further support for the bore interpretation of the lidar data, with differences being less than 20%. Furthermore, an effective wave trapping mechanism due to the curvature associated with a low-level jet ahead of the bore was diagnosed from the local soundings at the 2.1-km level, in excellent agreement with the lidar observation of the level at which the disturbance began to rapidly attenuate with height.

The strength of this bore was shown to be substantially greater than that of any previously studied bore generated by a thunderstorm gust front. Air within a pronounced surface-based inversion was rapidly lifted by the bore nearly to the level of a midtropospheric

inversion. The sudden upward displacement of the mixing ratio surfaces in the lowest 2–3 km of the atmosphere by the 30-min averaged bore updraft of 0.7 m s^{-1} resulted in the formation of thick haze or scattered low clouds as diagnosed from the display of aerosol backscattering ratio. The lidar data also suggested that the volume of intensely mixed air resulting from passage of this strong bore became an elevated mixed layer as the gravity current later undercut this layer; this was further substantiated with the rawinsonde data. Thus, the net effects of the disturbances were to dramatically increase the depth of the moist layer and to mix moisture throughout the lowest 4 km of the atmosphere, moisture that had previously been present only in a highly stratified form in the lowest 2.5 km.

Effects of bore passage on the local atmospheric structure were further assessed by applying a parcel displacement profile determined from the Raman lidar measurements to the prebore front sounding. Maximum displacements of 1.3 km resulted in substantial moistening, destabilization, and weakening of a capping inversion, yet the strong lifting was confined to too shallow of a layer near the surface to trigger deep convection. Results from this study suggested a number of considerations for determining the ability of such boundary-layer disturbances to be effective at releasing the potential instability of the atmosphere.

This study has shown the potential of the Raman lidar to study mesoscale meteorological phenomena. With the anticipated development of a daytime sensing capability, this system should be able to resolve important structures, such as the dryline, sea breezes, and topographically forced circulations. Perhaps its greatest utility will be discovered when it is implemented in multiscale research field programs, which can greatly aid in the interpretation of the vertical structures seen in the lidar data. Development and deployment of several such systems in a small region covered by other remote sensing systems for monitoring winds and temperatures in the lower atmosphere should be sought in the future for studies related to the hydrological budget.

Acknowledgments. The authors wish to express their sincere thanks to James Rottman and Richard Fulton for their thorough reviews of this paper, and to Harold Pierce for his assistance in processing the satellite imagery.

APPENDIX

Gravity-Current Depth Equation

An estimate for the depth of the cold air contained within the gravity current can be derived from the hydrostatic relation, assuming that the observed pressure rise associated with passage of the gravity current is entirely a hydrostatic consequence of the cooling. Consider an atmosphere at rest in approximate hydrostatic balance, as shown in Fig. A1. The observed surface pressure, virtual temperature, and layer-mean density of the cold air behind the leading edge of the gravity current are respectively denoted p_c, T_c, and ρ_c. The respective variables in the warm air mass ahead of the current are denoted p_w, T_w, and ρ_w. The depth of the gravity current d_o is defined as that height where the pressure p_d is uniform across the domain, since it is there that the temperature contrast reduces to a negligible value. Application of the hydrostatic law for the cold and warm air masses then gives, respectively:

$$dp\Big|_{p_c}^{p_d} = -\rho_c g dz\Big|_o^{d_o} \tag{A1}$$

$$dp\Big|_{p_w}^{p_d} = -\rho_w g dz\Big|_o^{d_o}, \tag{A2}$$

which can be manipulated to find an expression for the hydrostatic surface pressure difference between the two air masses,

$$\Delta p = p_c - p_w = g d_o(\rho_c - \rho_w), \tag{A3}$$

and thus the depth of the gravity current,

$$d_o = \frac{\Delta p}{g(\rho_c - \rho_w)}. \tag{A4}$$

The expression for the density difference is derived from the equation of state, upon assuming that the density difference at the surface is an adequate reflection of that within the entire depth of the gravity current, and that the current does not produce buoyancy variations in the ambient atmosphere:

$$\rho_c - \rho_w = \frac{p_c}{RT_c} - \frac{p_w}{RT_w} = \frac{\rho_w}{T_c}\left[\left(\frac{p_c}{p_w}\right)T_w - T_c\right]. \tag{A5}$$

Substitution of (A5) into (A4) produces the desired form of the expression for the gravity current depth, which uses only measurable surface variables:

$$d_o = \frac{T_c \Delta p}{\rho_w g[(p_c/p_w)T_w - T_c]}. \tag{A6}$$

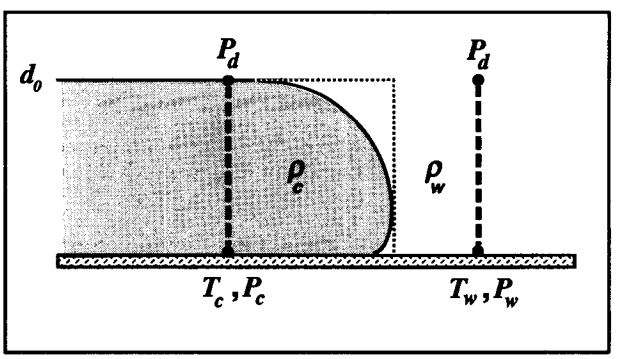

FIG. A1. Schematic diagram of a gravity current (shaded) in an unstratified environment with depth d_o and uniform density distribution. Other symbols are as defined in text.

REFERENCES

Bedard, A. J., and M. J. Saunders, 1978: Thunderstorm-related wind shear detected at Dulles international airport. Preprints, *Seventh Conference on Weather Forecasting and Analysis and Aviation Meteorology,* Boston, Amer. Meteor. Soc., 347–352.

Carbone, R. E., 1982: A severe frontal rainband. Part I: Stormwide hydrodynamic structure. *J. Atmos. Sci.,* **39,** 258–279.

——, J. W. Conway, N. A. Crook and M. W. Moncrieff, 1990: The generation and propagation of a nocturnal squall line. Part I: Observations and implications for mesoscale predictability. *Mon. Wea. Rev.,* **118,** 26–49.

Charba, J., 1974: Application of gravity current model to analysis of squall-line gust front. *Mon. Wea. Rev.,* **102,** 140–156.

Christie, D. R., K. J. Muirhead and A. L. Hales, 1978: On solitary waves in the atmosphere. *J. Atmos. Sci.,* **35,** 805–825.

——, —— and ——, 1979: Intrusive density flows in the lower troposphere: A source of atmospheric solitons. *J. Geophys. Res.,* **84,** 4959–4970.

Clarke, R. H., R. K. Smith and D. G. Reid, 1981: The morning glory of the Gulf of Carpentaria: An atmospheric undular bore. *Mon. Wea. Rev.,* **109,** 1726–1750.

Crook, N. A., 1986: The effect of ambient stratification and moisture on the motion of atmospheric undular bores. *J. Atmos. Sci.,* **43,** 171–181.

——, 1988: Trapping of low-level internal gravity waves. *J. Atmos. Sci.,* **45,** 1533–1541.

desJardins, M. L., and R. A. Petersen, 1983: GEMPAK: An interactive meteorological display and analysis system. Preprints, *Ninth Conference on Aerospace and Aeronautical Meteorology,* Boston, Amer. Meteor. Soc., 55–59.

Doviak, R. J., and R. Ge, 1984: An atmospheric solitary gust observed with a doppler radar, a tall tower and a surface network. *J. Atmos. Sci.,* **41,** 2559–2573.

Duchon, C. E., 1979: Lanczos filtering in one and two dimensions. *J. Appl. Meteor.,* **18,** 1016–1022.

Fulton, R., D. S. Zrnic and R. J. Doviak, 1990: Initiation of a solitary wave family in the demise of a nocturnal thunderstorm density current. *J. Atmos. Sci.,* **47,** 319–337.

Fujita, T., 1963: Analytical mesometeorology: A review. *Meteor. Monogr.,* Amer. Meteor. Soc., No. 27, 77–125.

Goff, R. C., 1976: Vertical structure of thunderstorm outflows. *Mon. Wea. Rev.,* **104,** 1429–1440.

Haase, S. P., and R. K. Smith, 1984: Morning glory wave clouds in Oklahoma: A case study. *Mon. Wea. Rev.,* **112,** 2078–2089.

——, 1989a: The numerical simulation of atmospheric gravity currents. Part I: Neutrally stable environments. *Geophys. Astrophys. Fluid Dynamics,* **46,** 35–51.

——, 1989b: The numerical simulation of atmospheric gravity currents. Part II: Environments with stable layers. *Geophys. Astrophys. Fluid Dynamics,* **46,** 35–51.

Hasler, A. F., and M. L. desJardins, 1987: AOIPS/2: An interactive system to process, analyze, and display meteorological data sets for nowcasting. *Adv. Space Res.,* **7,** 375–388.

Jenkins, G. M., and D. G. Watts, 1968: *Spectral Analysis and Its Applications.* Holden-Day, 525 pp.

Kaiser, J. F., and W. A. Reed, 1977: Data smoothing using low-pass digital filters. *Rev. Sci. Instrum.,* **48,** 1447–1457.

Koch, S. E., 1984: The role of an apparent mesoscale frontogenetical circulation in squall line initiation. *Mon. Wea. Rev.,* **112,** 2090–2111.

——, 1988: Mesoscale modeling of the severe thunderstorm environment. Preprints, *15th Conference on Severe Local Storms and Eighth Conference on Numerical Weather Prediction,* Boston, Amer. Meteor. Soc., J42–J51.

——, and J. McCarthy, 1982: The evolution of an Oklahoma dryline. Part II: Boundary-layer forcing of mesoconvective systems. *J. Atmos. Sci.,* **39,** 237–257.

——, and R. Golus, 1988: A mesoscale gravity wave event observed during CCOPE. Part I: Multiscale statistical analysis of wave characteristics. *Mon. Wea. Rev.,* **116,** 2527–2544.

Marks, J., 1974: Acoustic radar investigations of boundary layer phenomena. NASA Tech. Report CR-2432, Marshall Space Flight Center, Huntsville, AL, 65 pp [NTIS N7423183].

Maxworthy, T., 1980: On the formation of nonlinear internal waves from the gravitational collapse of mixed regions in two and three dimensions. *J. Fluid Mech.,* **96,** 47–64.

McAllister, L. G., 1968: Acoustic sounding of the lower troposphere. *J. Atmos. Terr. Phys.,* **30,** 1439–1444.

Melfi, S. H., and D. Whiteman, 1985: Observation of lower-atmospheric moisture structure and its evolution using a Raman lidar. *Bull. Amer. Met. Soc.,* **66,** 1288–1292.

——, —— and R. Ferrare, 1989: Observation of atmospheric fronts using Raman lidar moisture measurements. *J. Appl. Meteor.,* **28,** 789–806.

Nakane, H., and Y. Sasano, 1986: Structure of a sea-breeze front revealed by a scanning lidar observation. *J. Met. Soc. Japan,* **64,** 787–792.

Purdom, J. F. W., 1982: Subjective interpretations of geostationary satellite data for nowcasting. *Nowcasting,* K. Browning, Ed., Academic Press, 149–166.

Rottman, J. W., and J. E. Simpson, 1989: The formation of internal bores in the atmosphere: A laboratory model. *Quart. J. Roy. Meteor. Soc.,* **115,** 941–963.

Scott, R. W., and B. Ackerman, 1983: Surface signatures of a dry nocturnal gust front. *Mon. Wea. Rev.,* **111,** 197–204.

Seitter, K. L., 1983: The effect of arc cloud generation on thunderstorm gust front motion. Preprints, *13th Conference on Severe Local Storms,* Boston, Amer. Meteor. Soc., 249–252.

——, and H. S. Muench, 1985: Observation of a cold front with rope cloud. *Mon. Wea. Rev.,* **113,** 840–848.

Shapiro, M. A., 1984: Meteorological tower measurements of a surface cold front. *Mon. Wea. Rev.,* **112,** 1634–1639.

——, T. Hampel, D. Rotzoll and F. Mosher, 1985: The frontal hydraulic head: A micro-α scale ($\sim$1 km) triggering mechanism for mesoconvective weather systems. *Mon. Wea. Rev.,* **113,** 1166–1183.

Shreffler, J. H., and F. S. Binkowski, 1981: Observation of pressure jump lines in the Midwest, 10–12 August 1976. *Mon. Wea. Rev.,* **109,** 1713–1725.

Simpson, J. E., 1987: *Gravity Currents: In the Environment and the Laboratory.* John Wiley & Sons, 244 pp.

Smith, R. K., 1988: Travelling waves and bores in the lower atmosphere: The "Morning Glory" and related phenomena. *Earth-Science Reviews,* **25,** Elsevier Science, 267–290.

——, and M. J. Reeder, 1988: On the movement and low-level structure of cold fronts. *Mon. Wea. Rev.,* **116,** 1927–1944.

Wakimoto, R. M., 1982: The life cycle of thunderstorm gust fronts as viewed with Doppler radar and rawinsonde data. *Mon. Wea. Rev.,* **110,** 1060–1082.

Wilson, J. W., and W. E. Schreiber, 1986: Initiation of convective storms at radar-observed boundary-layer convergence lines. *Mon. Wea. Rev.,* **114,** 2516–2536.